QUANTUM INTERFERENCE BETWEEN SINGLE PHOTONS FROM A SINGLE ATOM AND A COLD ATOMIC ENSEMBLE

SANDOKO KOSEN

NATIONAL UNIVERSITY OF SINGAPORE

2014

QUANTUM INTERFERENCE BETWEEN SINGLE PHOTONS FROM A SINGLE ATOM AND A COLD ATOMIC ENSEMBLE

SANDOKO KOSEN
(B.Sc (Hons), NUS)

A THESIS SUBMITTED

FOR THE DEGREE OF MASTER OF SCIENCE
DEPARTMENT OF PHYSICS
NATIONAL UNIVERSITY OF SINGAPORE

2014

DECLARATION

I hereby declare that the thesis is my original work and it has been written by me in its entirety. I have duly acknowledged all the sources of information which have been used in the thesis.

This thesis has also not been submitted for any degree in any university previously.

SANDOKO KOSEN

5^{th} August 2014

Acknowledgements

This work would not have been possible without the help of everyone that worked on the single atom and atomic ensemble setups. Special thanks to Victor that has been a good company in the single atom setup for the last one year. I was clueless of experimental atomic physics (and by extension, everything else) when I first entered the lab. He introduced me to atomic physics, bash shell scripting, his favourite awk one-liners, electronics, etc. I will never forget the days we went through when we had problems with the vacuum chamber pressure and the MOT. Many thanks to Bharath and Gurpreet that worked in the atomic ensemble setup. Without Bharath's idea, my master thesis would still probably be about Raman cooling (which is an interesting subject as well).

To my thesis supervisor Professor Christian Kurtsiefer, he has been a great source of inspiration. He built an excellent research group here in NUS and instilled a very good research culture in the group. I thank you for accommodating me into your research group.

To everyone else in the quantum optics group: Brenda, Alesandro, Gleb, Wilson, Nick, Mathias Steiner, Matthias Seidler, Kadir, Chi Huan, Siddarth, (Spanish) Victor, Peng Kian, Hou Shun, and Yi Cheng. Thank you for making my stay enjoyable.

To all my family members, especially my parents, that are always there and have always cared for me. No words can express my gratitude to all of you.

At last, many thanks to all of the ^{87}Rb atoms that were once loaded into the optical dipole trap. You are the real unsung heroes. Without you, my thesis would probably stop at Chapter 1.

☺

Contents

Summary

Interfacing different physical systems is important for building a practical quantum information network as it can bring together the best features of each physical system. As a first step towards achieving this goal, we report on the observation of the Hong-Ou-Mandel (HOM) interference between the two single photons produced by two different physical systems. One single photon (6 MHz bandwidth) is produced through spontaneous emission from a single ^{87}Rb atom in an optical dipole trap. Another single photon (10 MHz bandwidth) is produced based on the detection of one photon in a time-correlated photon pair produced via a four-wave mixing process in a cold atomic ensemble of ^{87}Rb. In the first measurement, the two photons are made to arrive together at a 50:50 beam splitter. The coincidence measurements between detectors at the two outputs of the beam splitter shows an uncorrected interference visibility of 57±3% (corrected for background: 74±3%). We also examine the HOM effect for different time delays between the two photons as well as for different bandwidth of the atomic ensemble photon, and show that the behaviour agree with the theory.

List of Figures

LIST OF FIGURES

1

Introduction

Research in the field of quantum information has paved the path towards enhanced capabilities in the field of computation [1] and communication [2]. This emerging field of quantum computation and communication promises to perform tasks beyond what is possible using conventional technology[1]. To make use of this, one can think of a quantum network [4], that consists of multiple quantum nodes scattered across the network and interconnected by quantum channels. In each quantum node, the quantum information is produced, processed, and stored while it is reliably transferred between the nodes and eventually across the network through the quantum channels.

One feasible design of quantum network would be to use light as the physical system that implements the quantum channel. It can travel very fast and does not decohere easily, making it suitable as the carrier of quantum information. The difficulty, however, lies in choosing the right physical system to implement the quantum node. This is because different quantum nodes are expected to serve different purposes, such as photon sources, quantum memory, perform quantum gate operation, etc. Several good candidates are trapped ions [5], trapped atoms [6, 7], nitrogen-vacancy centres [8], quantum dots [9], etc. Contrary to photons, these systems allow to implement universal two-qubit operations, out of which a more complex algorithm can be composed.

It is very likely that a future implementation of quantum network may involve different physical systems in different quantum nodes to make the most out of each

[1]For instance, the Shor factorisation algorithm [3], if run on a quantum computer, would be able to break through the security of the public-key encryption schemes, such as the RSA scheme which is widely used in the internet nowadays

physical system. In an effort to realise a practical quantum network, it is therefore important to be able to efficiently interface different physical systems.

With the photon as the interconnect, the implementation may require the different physical systems to produce indistinguishable photons which is an important element in linear optics based quantum computation [10]. Yet, different physical systems produce single photons that are usually not indistinguishable. The indistinguishability between the two single photons can be demonstrated through the Hong-Ou-Mandel (HOM) interference experiment [11]. Hong et al. showed that two indistinguishable photons impinging on a 50:50 beam splitter will coalesce into the same, yet random, output port of the beam splitter.

The HOM interference has been demonstrated with single photons produced by the same kind of sources such as parametric down-conversion (PDC) [11, 12, 13], neutral atoms [14, 15], quantum dots [16, 17], single molecules [18, 19], ions [20], atomic ensembles [21], nitrogen-vacancy centres in diamond [22], and superconducting circuits [23]. To date, however, there are only two experiments demonstrating the HOM interference with single photons produced by two different physical systems: between a quantum dot and a PDC source [24], and between a periodically-poled lithium niobate waveguide and a microstructured fiber [25]. These experiment, however, rely on spectral filters to match the photons bandwidths.

In this thesis, we present the two-photon interference experiment with single photons produced by a single ^{87}Rb atom and a cold ^{87}Rb atomic ensemble without any use of spectral filtering. The single atom produces a single photon through spontaneous emission after excitation by a short optical pulse. The cold atomic ensemble produces narrowband time-correlated photon pairs through a four wave mixing process [26]. The detection of one photon in the photon pair heralds the existence the other "single" photon. We were able to experimentally observe a high HOM interference visibility.

The organisation of this thesis is as follows: Chapter 2 presents the two single photon sources used in the two-photon interference experiment. The discussion will be focused more on the single photon generation from the single atom system which constitutes the core part of my work. Chapter 3 presents the two-photon interference experiment for different time delays between the two single photons and for different atomic ensemble photon bandwidth.

2

Single Photon Sources

2.1 Introduction

A single photon can be defined in several ways. In standard quantum optics textbooks [27, 28], a single photon is the state resulting from a creation operator acting on the vacuum state. The usual example would be a single photon in a single frequency mode ($|1_\omega\rangle = \hat{a}(\omega)^\dagger|0\rangle$). This single photon state is very commonly used because it is simple from the pedagogical point of view and often sufficient to describe many of the quantum optics phenomena. However, being a single frequency mode implies that it is also delocalised in time. This is incompatible with the single photon produced in the laboratory that is localised in time (e.g. from spontaneous emission) and thus has a finite bandwidth[1]. A more practical definition would relate it to the detection process, or the generation process [29]. For instance, a single photon can be defined as a single "click" in the detector. The following discussion treats the single photon from the generation process point of view.

Over the last two decades, the major technological development in making a versatile single photon source is largely motivated by the emerging field of quantum information science. For instance, the first quantum cryptography protocol, BB84 [30, 31], requires a single photon source. Although the subsequent development of quantum cryptography protocols relaxes this requirement [32], it continues to find applications

[1] To incorporate the frequency distribution, one can define a single photon state as $|1_\beta\rangle = \int d\omega\beta(\omega)\hat{a}(\omega)^\dagger|0\rangle$, where $\beta(\omega)$ is the frequency distribution. This leads to the definition of a single photon with a frequency bandwidth.

in other fields, such as random number generation [33, 34], linear optics based quantum computation [10], quantum metrology [35, 36], etc.

Various single photon sources[1] are based on single quantum systems that can be optically or electrically excited, such as Nitrogen-Vacancy center in diamond, single ion, single atom, etc., and can be classified into the so-called deterministic source because they can, in principle, emit a single photon on demand. Another type of source relies on the generation of correlated photon pairs. The detection of one photon of the pair signifies the existence of another photon of the pair. This process is called heralding. The correlated photon pairs can be created through parametric down conversion in a nonlinear crystal, or through four-wave mixing in an atomic ensemble. This type of source is called a probabilistic source as the photon pair generation itself is probabilistic. However, as we shall see later, imperfection in the experimental setup easily introduces loss that severely limits the single photon generation efficiency from a deterministic source to only few percent. In this limit, there is not much difference between a deterministic and a probabilistic source.

There are two sources of single photons developed in our lab: a single trapped ^{87}Rb atom, and an ^{87}Rb atomic ensemble. The two-photon interference experiment presented in the next chapter uses single photons produced by these two sources. In the first system, the single atom emits a single photon through spontaneous emission after well-defined excitation. In the second system, the atomic ensemble produces a heralded single photon from a narrowband time correlated photon pair produced via a four wave mixing process. We first present in detail the generation of a single photon from single atom. We will also briefly discuss the single photon generation from the atomic ensemble.

2.2 Single Photon from Single Atom

Single photon generation from a single atom in cavity has been previously demonstrated for Rb [38, 39, 40, 41] and Cs [42]. Basically, the method made use of the Λ-type energy level scheme that consists of one excited state and two metastable ground states ($|g_1\rangle$ and $|g_2\rangle$). The pump laser and the cavity drive a vacuum-stimulated Raman adiabatic passage so that atom initially at $|g_1\rangle$ ends up at $|g_2\rangle$, emitting a single photon in

[1] A comprehensive review on single photon sources and detectors can be found in [37]

the cavity mode. Single photon generation from a Rb atom in free space has been demonstrated by [43] where the atom is excited along a closed cycling transition such that it generates a single photon through spontaneous emission. We adopt the latter approach in generating a single photon due to its similarity to our system although the details of the implementation are different.

The following sections describe the method employed in our single atom system to generate a single photon for the two-photon interference experiment.

2.2.1 Excitation of a Single Atom

There are several methods that can be used to excite an atom. Since there is a closed cycling transition in ^{87}Rb atom, we can approximate the atom as an effective two-level system. The electric dipole interaction between a two-level system and a resonant light of constant amplitude gives rise to the atom being put in the superposition state between the ground and the excited state with the probability amplitudes that depend on the amplitude of the electric field, the dipole matrix element and the duration of interaction[1]. The atom will continue to oscillate between the ground and excited state as long as it is interacting with the excitation light. This is commonly referred to as the Rabi oscillation. A square resonant pulse with the correct duration and power can completely transfer the state of the atom from the ground state to the excited state[2]. This is referred to as the π-pulse.

Alternatively, an optical pulse with an exponentially rising envelope can be used to excite the atom [44]. It has been demonstrated that this leads to a more efficient excitation in the sense that the average number of photons required is less than the one needed in the case of a square pulse. The drawback of this method is that the generation of an exponentially rising optical pulse is fairly complicated that involves the filtering of the optical sideband from an electro-optic phase modulator.

Another method to excite the atom is through adiabatic rapid passage (ARP) via chirped pulses [45, 46]. In this method, frequency of the excitation light is initially tuned below (or above) resonance and adiabatically swept through the resonance. The process has to be much faster than the lifetime of the excited state and at the same time has to be slow enough such that the atom is still able to follow the change adiabatically.

[1] Refer to Appendix B.1

[2] This does not take into account the spontaneous decay of the excited state.

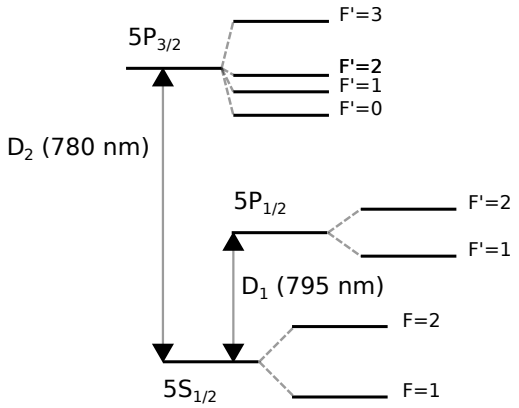

Figure 2.1: Energy level diagram of ^{87}Rb showing the $5S_{1/2}$ ground state, the $5P_{1/2}$ and $5P_{3/2}$ excited states and their corresponding hyperfine sublevels. Diagram not drawn to scale.

The advantage of ARP is that it is insensitive to the position of the atom as well as the intensity fluctuation of the excitation light. This is not the case for the π-pulse excitation method. The downside of ARP is that it requires extremely fast chirp and more power than a π-pulse.

In our single atom system, we choose to use the π-pulse excitation method with a square pulse because it is easier to deal with as compared to the other two methods mentioned above.

2.2.2 Basics of Single Atom Setup

Strong atom-light interaction has been achieved in the atom-cavity setting by using very high-finesse cavity [47]. However the high reflectivity nature of the cavity and the tremendous experimental effort required to realise such system make it not feasible to be scaled up in the context of a quantum network. Our setup adopts another approach where we trap a single atom in the free space setting. Substantial atom-light interaction is achieved [48] by strongly focusing the probe laser beam to a diffraction-limited spot size as illustrated in Fig. 2.2. The basic setup consists of two confocal aspheric lenses with effective focal length of 4.5 mm (at 780 nm) enclosed in an ultra high vacuum chamber. The lenses are designed to transform a collimated laser beam into a diffraction-limited spot size at the focus of the lens with minimal spherical aberration.

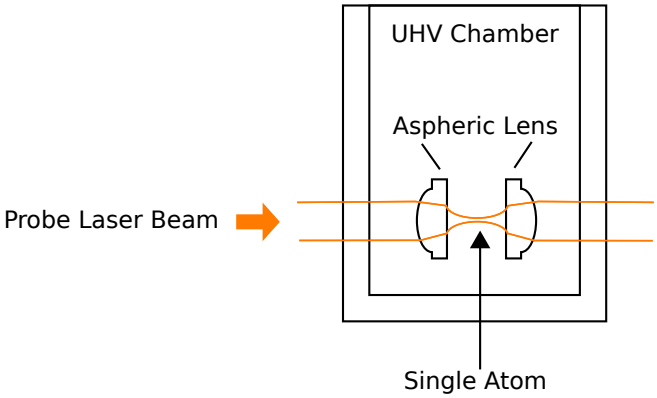

Figure 2.2: Strong atom-light interaction achieved through strong focusing.

To trap a single atom, we start with an atomic cloud in a magneto-optical trap (MOT) and use an optical dipole trap to trap a single atom at the focus of the lens[1].

A MOT consists of three pairs of counter-propagating laser beams that intersect at the center of a quadrupole magnetic field. The quadrupole field is created by a pair of anti-Helmholtz coils, while three other orthogonal pairs of Helmholtz coils are used to compensate for stray magnetic fields (coils not shown in Fig. 2.2). The MOT is used to capture the slow atoms and cool them down further into the centre of the quadrupole field.

In describing the fine structure of ^{87}Rb, we use the standard notation nL_J in atomic physics where n denotes the principal quantum number, L the total orbital angular momentum quantum number, and J the total electron angular momentum quantum number. Two important transitions relevant to the single atom setup are (Fig. 2.1): $5S_{1/2} \rightarrow 5P_{1/2}$ (D_1 line, $\approx 795\,\text{nm}$) and $5S_{1/2} \rightarrow 5P_{3/2}$ (D_2 line, $\approx 780\,\text{nm}$). To describe the hyperfine interaction between the electron and the nuclear angular momentum I, we denote $F = J + I$ as the total atomic angular momentum quantum number.

Each MOT laser beam consists of a cooling beam red detuned (to compensate for the Doppler shift) by ≈ 24 MHz from the $|5S_{1/2}, F = 2\rangle \rightarrow |5P_{3/2}, F' = 3\rangle$ transition and a repump beam tuned to the $|5S_{1/2}, F = 1\rangle \rightarrow |5P_{1/2}, F' = 2\rangle$ transition. The MOT cooling beam cools the atomic cloud. Off-resonant excitation induced by the MOT cooling beam may cause the atoms to decay to the $|5S_{1/2}, F = 1\rangle$ ground state. The MOT repump beam empties the $|5S_{1/2}, F = 1\rangle$ state by exciting it to $|5P_{1/2}, F' = 2\rangle$,

[1]For complete details on the operation of a MOT and optical dipole trap, refer to [46]

from which the atoms can decay back to the $|5S_{1/2}, F = 2\rangle$ ground state and continue to participate again in the cooling process. The typical power of each MOT cooling beam is $\approx 150\,\mu$W while the total power of the MOT repump beams sum up to $\approx 150\,\mu$W.

The optical dipole trap is a far-off-resonant trap (FORT) that consists of a red detuned Gaussian laser beam at 980 nm (far detuned from the optical transitions of ^{87}Rb) that is focused by the aspheric lens (the same lens that focuses the probe beam). Therefore a large intensity gradient is created at the focus of the lens. As the dipole trap is red-detuned, the atom will be attracted towards the region with the highest intensity at the focus of the lens. In order to maintain a constant depth of the trapping potential, the power of the optical dipole trap is locked.

The optical dipole trap operates in the collisional blockade regime [49, 50]. As soon as there are two particles in the trap, the collision between the particles in the trap will become the dominant loss mechanism and kick both atoms out of trap. As such, there can either be only 0 or 1 atom in the trap. The presence of a single atom in the trap can be seen from the detection signal that jumps between two discrete levels. When there is no atom in the trap, the detector detects the background noise. With one atom in the trap, the detector detects a higher discrete level which is the atomic fluorescence. The presence of a single atom has also been independently verified by the measurement of the second-order autocorrelation function of the atomic fluorescence between two independent detectors ($g^{(2)}(\tau)$, where τ is the detection time delay between the two detectors). The value of the second-order autocorrelation function has been shown to drop below 0.5 at $\tau = 0$, which is the signature of a single emitter [48].

2.2.3 Resonance Frequency Measurement

Under the presence of the optical dipole trap beam, the energy levels of the trapped atom are shifted due to the AC-Stark shift. In order to achieve the highest excitation probability through the π-pulse excitation method, it is necessary that the optical frequency of the optical pulse to be on resonance with the optical transition. It is the purpose of this section to explain how this resonance frequency is determined. The idea is to send a weak probe beam to the trapped single atom and measure the transmitted power as a function of the probe beam optical frequency. As the optical frequency approaches the resonance frequency, the atom scatters more of the probe beam, resulting in a smaller transmission. The optical frequency that results in the

largest decrease in the transmission corresponds to the resonance frequency of the probed optical transition.

2.2.3.1 The Closed Cycling Transition

Fig. 2.3 shows the $|5S_{1/2}, F = 2, m_F = \pm 2\rangle \leftrightarrow |5P_{3/2}, F' = 3, m_{F'} = \pm 3\rangle$ transition in ^{87}Rb atom (D_2 line). Each of these transitions forms a closed cycling transition and can only be excited by probe beam circularly polarised with the correct handedness with respect to the quantisation axis we define for the atom. For instance, an atom initially prepared in $|5S_{1/2}, F = 2, m_F = +2\rangle$ excited by a σ_+ beam can only end up in $|5P_{3/2}, F' = 3, m_{F'} = +3\rangle$ of the excited state. This is because selection rule (conservation of angular momentum) only allows $\Delta m_F = +1$ transition. Upon decaying from $|5P_{3/2}, F' = 3, m_{F'} = +3\rangle$, the atom can only end up in $|5S_{1/2}, F = 2, m_F = +2\rangle$ due to the selection rule also ($\Delta F = 0, \pm 1$ and $\Delta m_F = 0, \pm 1$). The same reasoning applies to the $|5S_{1/2}, F = 2, m_F = -2\rangle \rightarrow |5P_{3/2}, F' = 3, m_{F'} = -3\rangle$ probed by a σ_- beam. Therefore, exciting ^{87}Rb atom along one of these transitions allows us to approximate a multi-level ^{87}Rb atom as an effective two-level system. In this work, we choose to excite the σ_- transition.

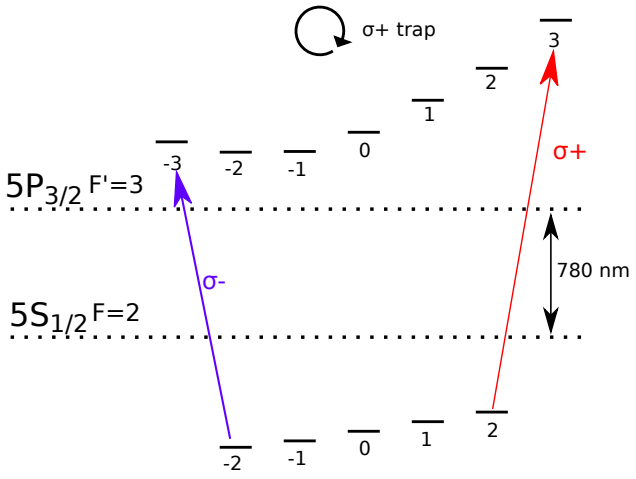

Figure 2.3: Energy level diagram of a single ^{87}Rb atom trapped in a far-off-resonance dipole trap showing the $F = 2$ to $F' = 3$ levels of the D_2 transition with their m_F sublevels. The different positions of the m_F sublevels are shifted by the AC Stark effect induced by the presence of σ_+ polarized dipole trap.

The above scheme works only if the probe beam is a true σ_- or σ_+ beam. However due to the imperfection in the experimental setup, the polarisation of the probe beam is

never perfect and that may cause an off-resonant excitation to other hyperfine levels of the excited state. This may cause the atom to subsequently decay to the $|5S_{1/2}, F = 1\rangle$ of the ground state and exit the closed cycling transition. To correct for this, another repump beam that is tuned to the $|5S_{1/2}, F = 1\rangle \rightarrow |5P_{1/2}, F' = 2\rangle$ transition is sent together with the probe beam. Its sole purpose is to empty the $|5S_{1/2}, F = 1\rangle$ state and populate the $|5S_{1/2}, F = 2\rangle$ state. In the following, we refer to this repump beam as the probe repump beam to distinguish it from the MOT repump beam.

In order to enter the closed cycling transition, the atom needs to be prepared in the ground state of the cycling transition, i.e. $|5S_{1/2}, F = 2, m_F = -2\rangle$. To do so, we perform optical pumping by sending a σ_- polarised beam tuned to the $|5S_{1/2}, F = 2\rangle \rightarrow |5P_{3/2}, F' = 2\rangle$ transition together with the probe repump beam. The optical pumping beam will only induce optical transition that satisfies $\Delta m_F = -1$ selection rule, while during spontaneous emission $\Delta m_F = 0, \pm 1$, $\Delta F = 0, \pm 1$. The probe repump beam ensures that the $|5S_{1/2}, F = 1\rangle$ is always empty. If this process continues for a while, atom will eventually end up in $|5S_{1/2}, F = 2, m_F = -2\rangle$. This is a "dark state" that is effectively decoupled from the optical pumping beam because there is no corresponding $|5P_{3/2}, F' = 2, m_{F'} = -3\rangle$.

2.2.3.2 Transmission Measurement

A schematic diagram of the experimental setup used in the transmission measurement is shown in Fig. 2.4.

The optical dipole trap beam uses a circular polarisation with a well-defined Gaussian spatial mode. As the presence of the dipole trap beam breaks the degeneracy of the m_F sub levels due to AC Stark shift, it is therefore convenient to describe the atom with a quantisation axis pointing along the z-axis parallel to the propagation direction of the optical dipole trap beam as shown in Fig. 2.4. With this quantisation axis, the optical dipole trap beam is σ_+ polarised. To further break the degeneracy, a bias magnetic field of 2 Gauss is generated at the location of the atom using a magnetic coil (not shown in Fig. 2.4).

All the laser beams except for the optical dipole trap laser beam pass through separate acousto-optic modulators (AOM) that allow fine tuning of frequency by changing the frequency of the radio frequency (RF) signal applied to the AOM. The RF signal is produced by a home made direct digital synthesiser (DDS). By changing the amplitude

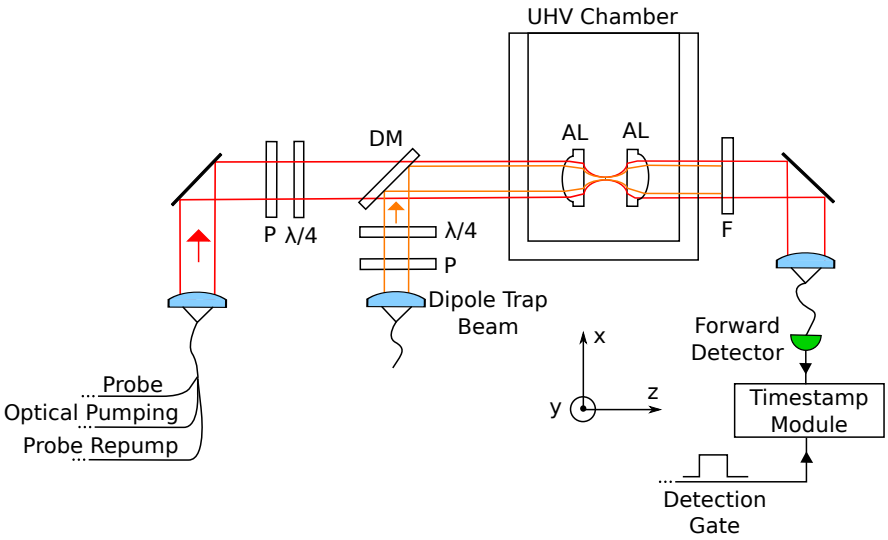

Figure 2.4: Experimental setup for the transmission experiment. P: polariser, $\lambda/4$: quarter-wave plate, DM: dichroic mirror, AL: aspheric lens, UHV Chamber: ultra high vacuum chamber, F: interference filter that transmits light at 780 nm.

of the RF signal, the AOM can also be used as a switch that controls if the beam is sent to the atom. The optical pumping beam, probe beam and probe repump beam are coupled into a single mode optical fiber so that they have a well-defined Gaussian spatial mode at the output of the optical fiber. The polariser and the quarter-wave plate is used to transform the incident beam into a σ_- polarised beam.

The forward detector is a passively-quenched silicon avalanche photodiode with a deadtime of about 3 μs and jitter time of about 1 ns. It is used to record the transmitted light during the transmission experiment. The timestamp module records the arrival time of each photon detected by the photodetector with a timing resolution of about 125 ps.

The whole experiment is controlled by a pattern generator that receives a series of commands, i.e. experimental sequence, from the host computer and outputs a sequence of electrical signals that control the rest of the devices in the experimental setup. In particular, the system has also been configured to decide whether or not an atom is present in the trap based on the detection counts recorded by the forward detector.

The experimental sequence for the transmission experiment is as follows: (schematic shown in Fig. 2.5)

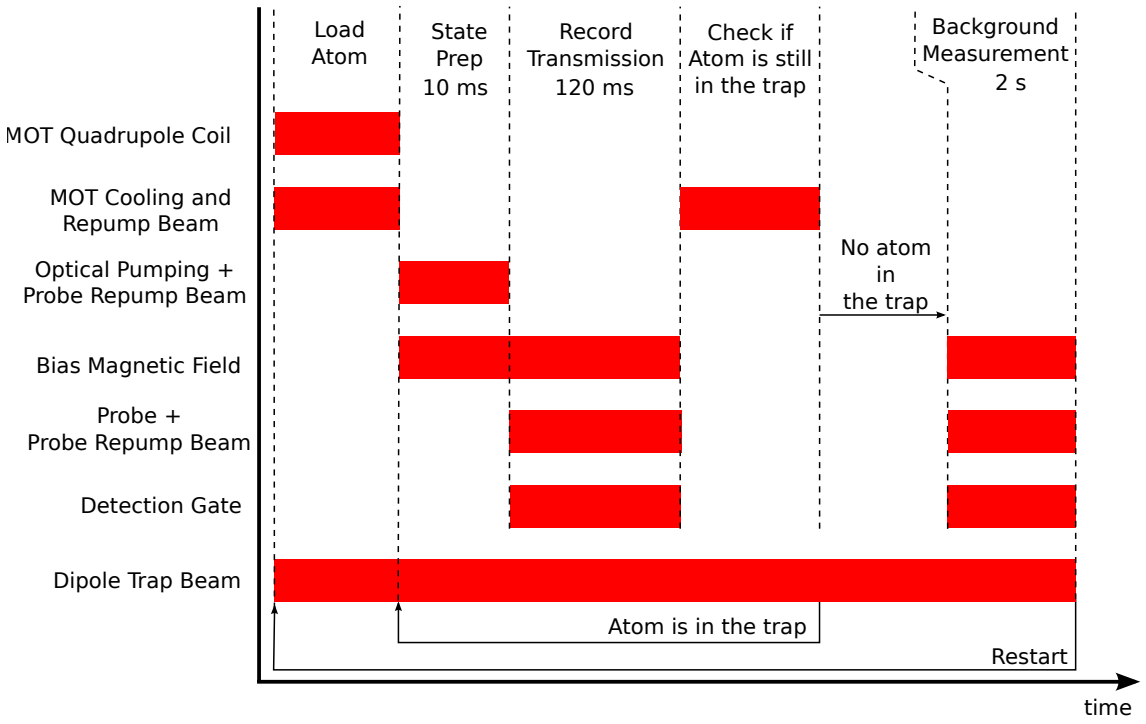

Figure 2.5: Schematic of the experimental sequence for the transmission experiment. Details in text.

1. Turn on MOT cooling and repump beams as well as the MOT quadrupole coil and wait for an atom loading signal from the forward detector. If the system determines that an atom is successfully loaded into the trap, then proceed to the next step.

2. Apply a bias magnetic field of 2 Gauss in the z direction at the site of the atom.

3. Perform state preparation by sending the optical pumping beam and the probe repump beam to the atom for 10 ms.

4. Turn off the optical pumping beam and turn on the probe beam. This is to allow some time for the optical pumping beam to be completely turned off and for the power of the probe beam to stabilise.

5. At this point in time the power of the probe beam has reached its steady state. The timestamp module starts recording the arrival time of each photon detected by the forward detector. This process lasts for 120 ms.

6. Turn off the magnetic field and the probe beam. Turn on the MOT cooling and MOT repump beams. Check for the presence of an atom based on the detection in the forward detector. If so, then repeat steps 2 to 6. Otherwise proceed to step 7 for background measurement.

7. At this point, there is no atom in the trap. Turn on the probe beam, probe repump beam and the magnetic field, wait for another 5 ms to allow them some time to stabilise.

8. The timestamp module starts recording the background signal in the forward detector in the absence of the atom. This process lasts for 2 s. At the end of the background measurement, return to step 1.

The background measurement gives the power level of the probe and probe repump beam in the absence of the atom. This is used as a reference that will be compared to the detected power in the presence of the atom.

This experimental sequence for different detuning of the σ_- probe beam with respect to the unperturbed transition frequency in the absence of any dipole trap beam and bias magnetic field. At each point, we measured the average transmission of the probe

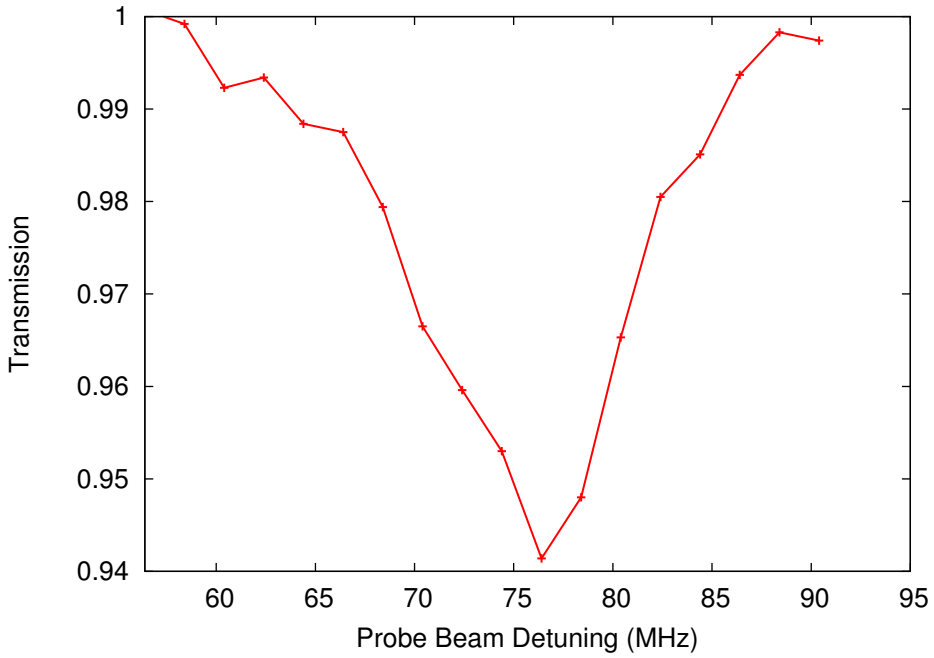

Figure 2.6: Average transmission of the (σ_-) probe beam across a trapped single ^{87}Rb atom measured as a function of its detuning with respect to the unshifted resonance frequency of $|5S_{1/2}, F = 2\rangle \rightarrow |5P_{3/2}, F' = 3\rangle$. The largest decrease in the transmission value corresponds to the resonance frequency of the probed optical transition ($|5S_{1/2}, F = 2, m_F = -2\rangle \rightarrow |5P_{3/2}, F' = 3, m_{F'} = -3\rangle$).

beam. The details on the averaging of the transmission value can be found in [48]. The result is shown in Fig. 2.6.

The lowest measured transmission is 94 % corresponding to 6 % extinction of the probe beam smaller than the 10 % extinction reported by [48] for the similar experimental setup. There are several reasons that can possibly explain this. Smaller input divergence of the probe beam can result in a weaker focusing by the aspheric lens. Any slight misalignment between the probe beam and the optical dipole trap beam can cause the probe beam to be focused at slightly different position from the focus of the optical dipole trap. These factors can result in a slightly different electric field amplitude experience by the atom that can in turn weaken the atom-light interaction.

Nevertheless, we have successfully observed a decrease in the transmission probe beam. The result shows that the resonance frequency of the $|5S_{1/2}, F = 2, m_F = -2\rangle \rightarrow |5P_{3/2}, F' = 3, m_{F'} = -3\rangle$ transition is found at 76 MHz blue-detuned from the natural

transition frequency.

2.2.4 Pulsed Excitation of a Single Atom

2.2.4.1 Overview of the Optical Pulse Generation

As the lifetime of the ^{87}Rb $|5S_{1/2}\rangle \rightarrow |5P_{3/2}\rangle$ is about 27 ns [51], the excitation process has to happen within a duration much smaller than this lifetime. Therefore, we need to generate a very short optical pulse, around 3 ns duration, with very well-defined edge as well (rise and fall time $\lesssim 1$ ns) to ensure that there is a clear separation between the spontaneous emission regime and the excitation process.

We employed a Mach-Zehnder based electro-optic modulator (EOM)[1] as the amplitude modulator. The EOM device consists of a DC bias port and an RF port. The DC bias is used to set the EOM to its minimum transmission point such that minimal amount of light is transmitted when there is zero voltage applied on the RF port. Upon the application of an electrical pulse on the RF port, the EOM transmits an optical pulse with the same duration as the electrical pulse.

As the light is on resonance with the probed optical transition, it is necessary to minimise the amount of light sent to the atom when there is no electrical pulse applied on the RF port. For that reason, we decided to use two EOMs in series in order to double the extinction ratio of the amplitude modulation. The extinction ratio can be further increased by switching off the AOM through the direct digital synthesiser unit. However, this can only be done if the time separation between the two consecutive pulses is larger than the response time of the AOM. In the following pulsed excitation experiment, the AOM is always on and we rely only on the two EOMs to reach high extinction ratio. The schematic diagram of the devices used in this optical pulse generation is shown in Fig. 2.7.

The optical output from the EOM depends on the shape of the electrical RF pulse that enters the RF port of the EOM. Therefore, the RF electrical pulse has to be a square pulse with the intended duration and well-defined edge. Fig. 2.7 illustrates the electrical pulse generation. The pattern generator generates an electrical pulse of 20 ns

[1] EOSPACE 20 GHz broadband with a promised extinction ratio of 21 dB. The extinction ratio is defined as follows: given an input with constant power, it is the ratio between the maximum and the minimum transmission of the amplitude modulator.

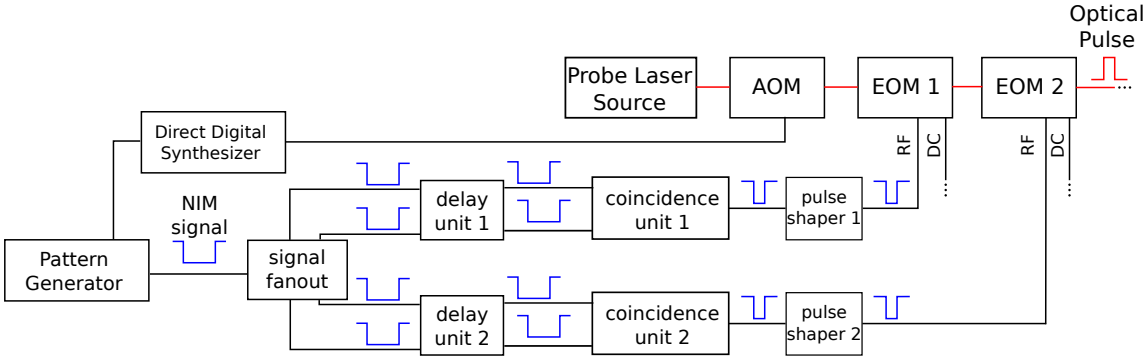

Figure 2.7: Schematic diagram of the optical pulse generation process from a continuous probe laser beam.

duration in the form of a NIM signal[1] that gets duplicated into four identical signals by a electronic fanout. The delay unit accepts two NIM signals and delays one of them with respect to the other with a resolution of ~ 10 ps. The coincidence unit acts as a coincidence gate that produces a new NIM signal with a duration defined by the relative delay of the input pulses. Finally it passes through a pulse-shaper unit that shortens the rise and fall time of the NIM signal to about 1 ns. The two EOMs are synchronised to work together by tuning the setting of each EOM's delay unit such that the electrical pulse that goes to EOM 2 arrives later than the one that goes to EOM 1.

2.2.4.2 Spontaneous Emission from a Single Atom

The experimental setup for this pulsed excitation experiment is shown in Fig. 2.8. This is almost similar to the setup used in the transmission measurement (Fig. 2.4) with the addition of a few components. In contrast to the weak coherent beam used in the transmission experiment, this experiment uses a strong coherent pulse to excite the atom. In order to reconstruct the optical pulse shape and at the same time to estimate the average number of photons in the optical pulse, a neutral density filter (NDF) is added just before the forward detector to prevent saturation due to the optical pulse. The value of the NDF is chosen such that on average only $\approx 1\%$ of the photons in the optical pulse reaches the forward detector. However, the presence of the NDF in the

[1] Acronym for Nuclear Instrumentation Method, with the following convention: voltage of -200 mV corresponds to digital 0 and -800 mV for digital 1.

forward detection arm also makes the single photon emission and the atom loading signal from the atom negligible. Therefore, another single photon detector is added in the setup as shown in Fig. 2.8 ("Backward Detector"). This detector will be the one used to record the single photon emission from the atom. In this experiment, the system will make a decision regarding the presence of an atom in the trap by triggering on the signal detected by the backward detector.

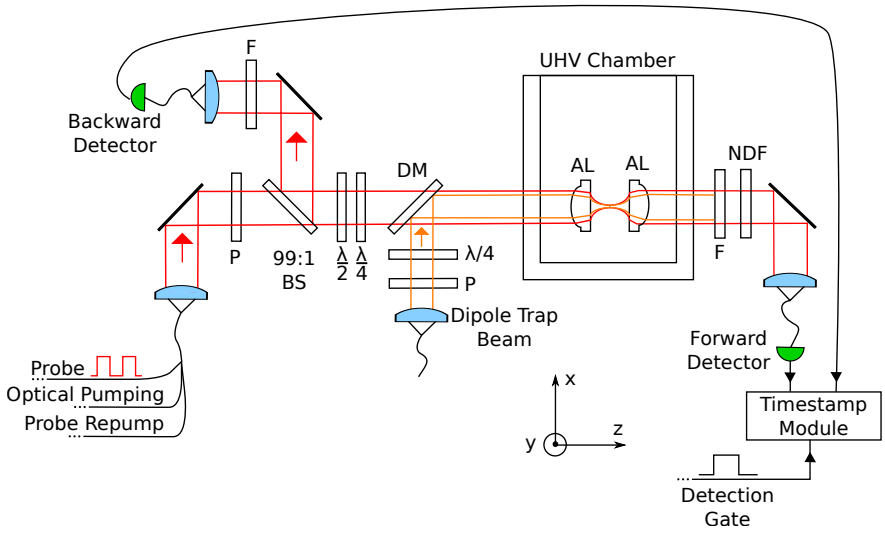

Figure 2.8: Experimental setup in the pulsed excitation experiment. P: polariser, $\lambda/2$: half-wave plate, $\lambda/4$: quarter-wave plate, 99:1 BS: beam splitter that reflects 99% and transmits 1% of the incident beam, DM: dichroic mirror, AL: aspheric lens, UHV Chamber: ultra high vacuum chamber, F: interference filter that transmits light at 780 nm, NDF: neutral density filter.

Fig. 2.9a shows an example of a 3 ns optical pulse reconstructed using the forward detector. As we are limited by the ~ 1 ns timing jitter of the detector, the data is processed in 1 ns timebins. The vertical axis represents the normalised counts at time t, $N(t)$, defined as

$$N(t) = \frac{\text{Number of clicks in the detector in 1 ns time bin at time } t}{\text{Number of optical pulses}} \tag{2.1}$$

The average number of photons per optical pulse at the location of the atom, N_p, can be estimated by measuring the area under the optical pulse shown in Fig. 2.9 and dividing it with the transmission factor from the location of the atom to the detector. We estimated a transmission factor of $(7 \pm 1) \times 10^{-5}$ (NDF ~37 dB, fiber

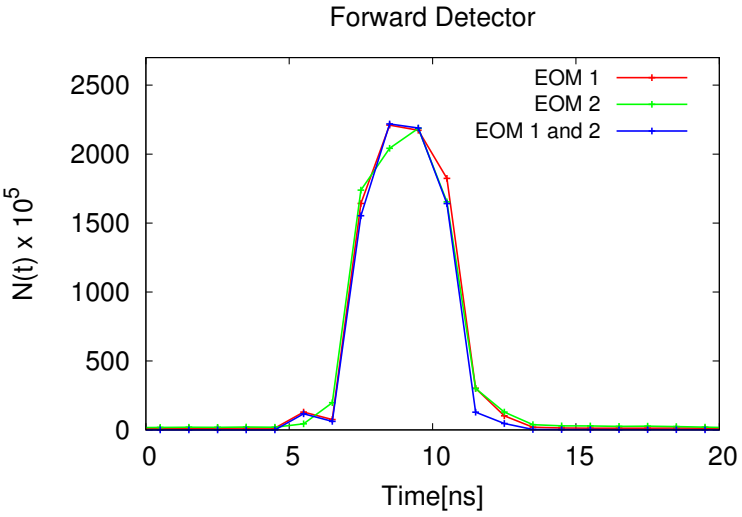

(a)

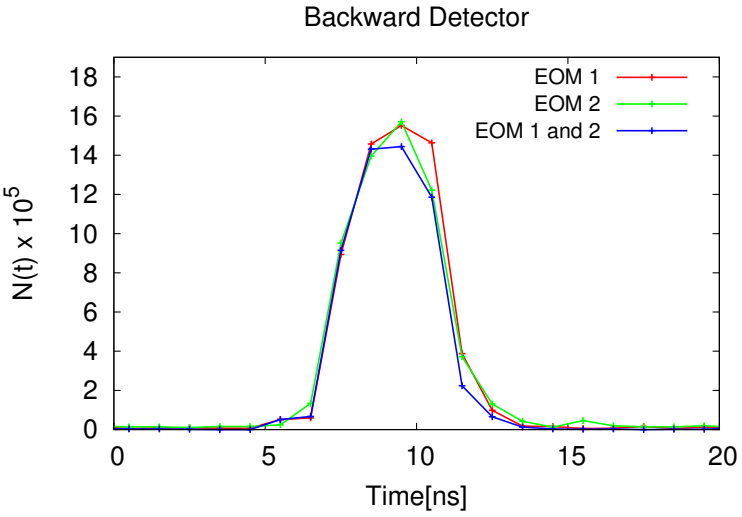

(b)

Figure 2.9: Optical pulse reconstructions in the forward and backward detectors. Both are passively-quenched avalanche photodiodes. (EOM1) the first EOM is used for modulation while the second EOM is set at the maximum transmission point. (EOM2) the second EOM is used for modulation while the first EOM is set at the maximum transmission point. (EOM 1 and 2) Both EOMs are used for modulation. The fact that the reconstructed optical pulses coincide with each other demonstrates that we have successfully synchronised the two EOMs.

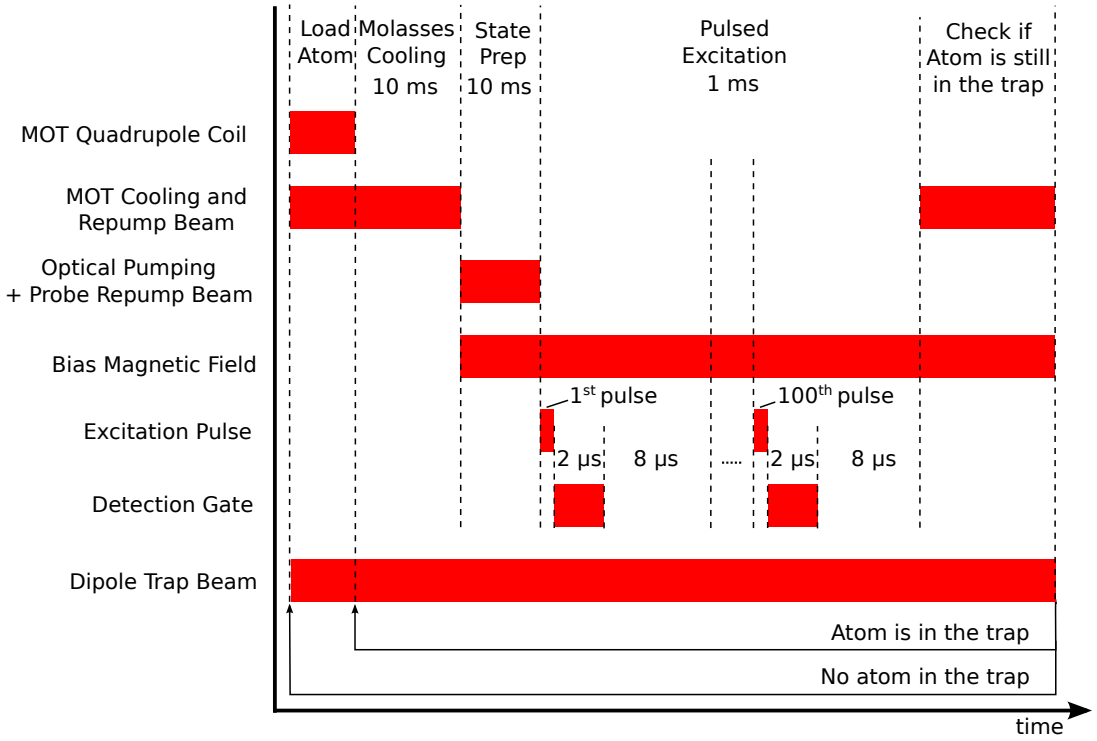

Figure 2.10: The experimental sequence for the pulsed excitation experiment. Details in text.

coupling efficiency ~ 70%, and detector quantum efficiency ~ 50%) for the measurement using the forward detector. This results in an average of ~ 1140±160 photons per optical pulse at the location of the atom for the example shown in Fig. 2.9a.

Fig. 2.9b indicates that there is a very small fraction of the optical pulse back-reflected towards the backward detector. We have verified that the back-reflection originates from the surface of an optical component located before the UHV chamber. The falling edge of this back-reflection will serve as the timing reference that marks the beginning of the spontaneous emission.

The experimental sequence for the pulsed excitation experiment is as follows (Fig. 2.10):

1. Load a single atom into the trap by triggering on the signal detected by the backward detector.

2. Perform molasses cooling for 10 ms to further cool down the atom in the trap.

3. Apply a small bias magnetic field of 2 Gauss in the z-direction. Perform state

preparation for 10 ms by sending the optical pumping and probe repump beams to the atom. This step prepares the atom in the $|5S_{1/2}, F = 2, m_F = -2\rangle$ state.

4. Send a signal to the EOMs to generate an optical pulse and let the timestamp module records the arrival time of each event detected in the forward as well in the backward detector for 2 μs.

5. Repeat step 4 every 10 μs for 100 times.

6. Check if the atom is still in the dipole trap. If so, then repeat steps 2 to 5. Otherwise, restart from step 1.

In this experiment the probe beam AOM is always turned on and we rely solely on the two EOMs to minimise the amount of the probe light outside the optical pulse.

Fig. 2.11 shows the detection events in the backward detector in the pulsed excitation experiment with a 3 ns resonant optical pulse. With the presence of an atom in the trap, the detector detects the spontaneously emitted single photon emission from the single atom with a characteristic decay time of 26.5 ± 0.5 ns in agreement with the results reported in the literature [52, 53, 54]. The probability of the atom being in the excited state after the excitation ($P_e(t)$) can be inferred from the value of $N(t)$ and is shown on the right hand axis of Fig. 2.11[1].

2.2.4.3 Rabi Oscillation

The total excitation probability, P_E, is extracted from the fluorescence data by integrating the normalised counts $N(t)$ under the spontaneous regime and dividing it by the overall detection and collection efficiency ($\eta_d \cdot \eta_s \approx 0.01$).

$$P_E = \frac{\int_{t_i}^{t_f} N(t)dt}{\eta_d \cdot \eta_s} = \frac{A(t_i, t_f)}{\eta_d \cdot \eta_s} \tag{2.2}$$

The beginning of the spontaneous emission regime is chosen to coincide with the falling edge of the optical pulse ($t_i = 0$) and t_f is chosen to be 155 ns corresponding to approximately $5.7\tau_e$ away from t_i, where $\tau_e = 27$ ns. The latter is motivated by the fact that for $t > t_f$, the noise is more dominant than the signal. In addition, $e^{-(t_f - t_i)/\tau_e} \approx 10^{-3}$ and the tail of the exponential decay starting from t_f only contributes about 0.1 % to

[1] Details on the conversion from $N(t)$ to $P_e(t)$ can be found at Appendix A.1

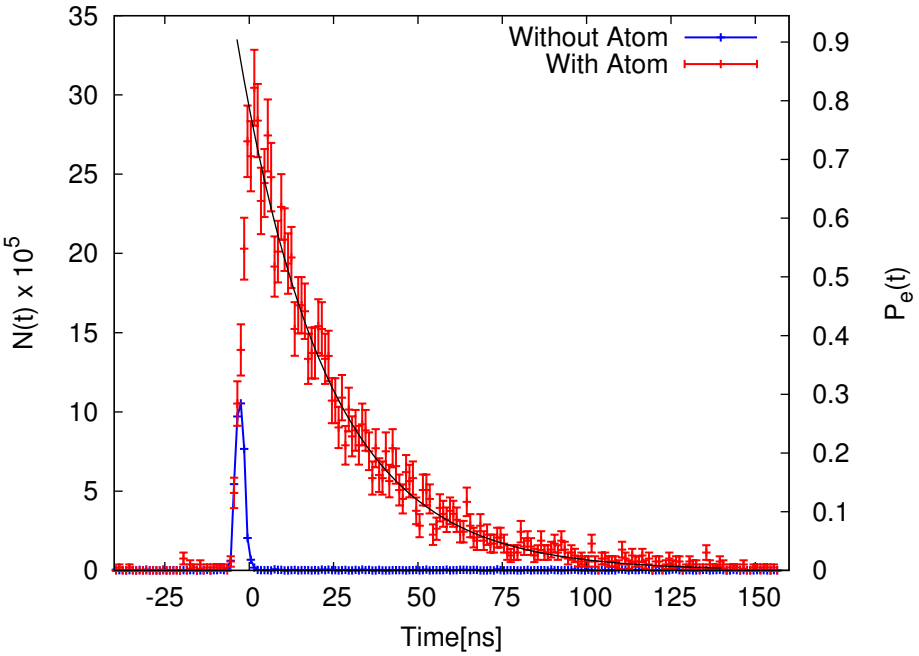

Figure 2.11: Spontaneous emission from a single atom. ("Without Atom") Detection events in the backward detector without atom in the trap. The detector measures the back-reflected optical pulse from the surface of an optical component located before the UHV chamber. ("With Atom") Detection results from the backward detector during the pulsed excitation experiment with an average of 700 photons per 3 ns optical pulse incident on the atom. The detector measures the atomic fluorescence as well as the back-reflected optical pulse. The left axis indicates the normalized counts, $N(t)$, and the right axis indicates the probability of the atom being in the excited state, $P_e(t)$ (refer to Appendix A.1). The displayed error bar is the standard deviation of each data point attributed to the Poissonian counting statistics. The black line is an exponential fit with a characteristic decay time of 26.5 ± 0.5 ns. All data are processed in 1 ns timebin.

the total excitation probability. This justifies the choice of neglecting the tail of this exponential decay.

We first performed the pulsed excitation experiment by varying the average number of photons per optical pulse (N_p) for a fixed 3 ns pulse duration and we measured the total excitation probability P_E for each data point. The purpose is to find the π-pulse which corresponds to the highest total excitation probability. Fig. 2.12a shows the Rabi oscillation of a single atom where the amplitude of the optical pulse is varied while the duration is kept constant. The total excitation probability reaches a maximum of $78 \pm 4\%$ [1]for $N_p = 700$. This is the π-pulse for a 3 ns optical pulse. The black dashed line in Fig. 2.12a is the theoretical fit of (2.3) to the data (refer to Appendix B.1).

$$P_E = \sin^2\left(\sqrt{N_p} \times \text{constant}\right) \tag{2.3}$$

For the same 3 ns π-pulse, we measured the Rabi oscillation of a single atom where the optical pulse duration is varied while keeping the same amplitude of optical pulse as shown in Fig. 2.12b. As expected the first maximum of the Rabi oscillation is found for a 3 ns pulse width which corresponds to the π-pulse. The excitation probability for the 2π-pulse does not reach zero as the spontaneous emission starts to take effect.

The parameter for this 3 ns π-pulse will be used to excite the single atom in the two-photon interference experiment presented in the next chapter.

2.3 Heralded Single Photon from Atomic Ensemble

In this section, we briefly discuss the generation of time-correlated photon pairs produced from a cold ^{87}Rb atomic ensemble developed in our group [26]. The time-correlated photon pair can be used to generate a heralded single photon state, i.e. the detection of one of the photon in the photon pair heralds the existence of another photon.

[1]The main reason for which we obtained a maximum of 78% is because the quantum efficiency of the single photon detector is assumed to be 0.5 in the calculation of P_E. We have independently verified that for the same value of N_p, we obtained a higher excitation probability (near to 1) by using another single photon detector while still assuming photo detection quantum efficiency of 0.5 in the calculation of P_E. The theoretical maximum is determined by the free decay of the excited state: $\frac{1}{2}\left(1 + e^{-3/27}\right) \approx 94.7\%$.

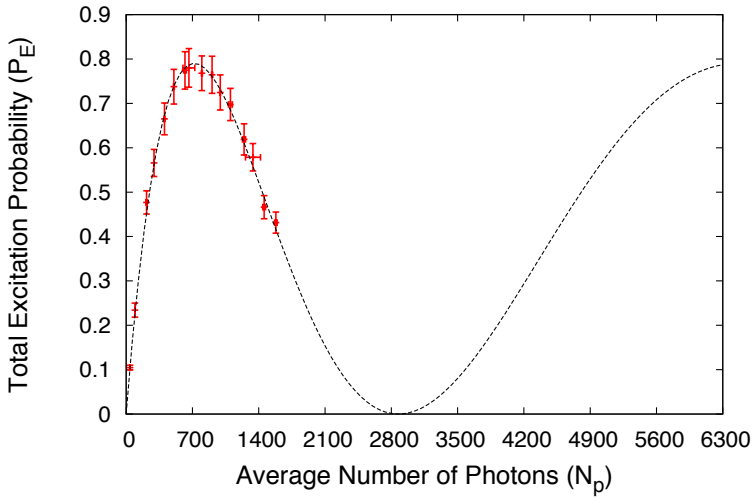

(a)

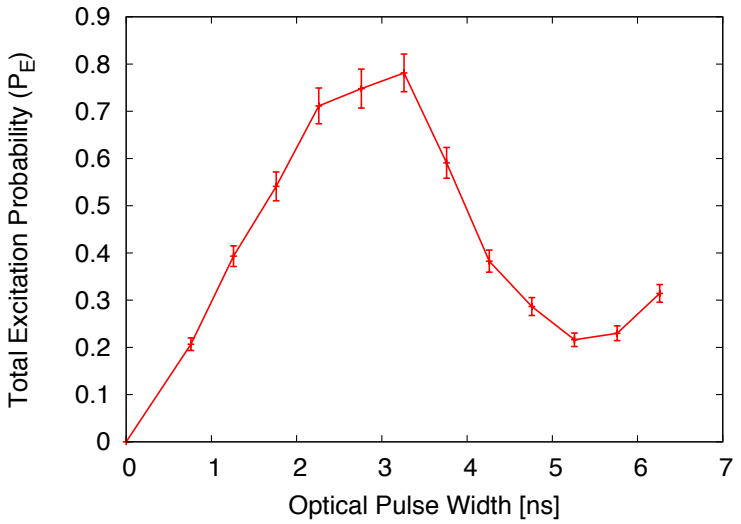

(b)

Figure 2.12: Rabi oscillation of a single atom. (a).(Red data points) Total excitation probability versus average number of photons per 3 ns optical pulse incident at the atom. There is no data point beyond N_p = 1600 as we are limited by the maximum power that can obtained from our laser. The uncertainty in N_p is the difference between average number of photons measured before and after each data point, mainly attributed to the drift in the power of the probe laser. (Dashed line) Fit of $A\sin^2(\sqrt{N_p}B)$ where A and B are the fitted parameters. Refer to (2.3) in the main text for more details. (b).Total excitation probability versus optical pulse width. The calculation of the uncertainty of P_E for both data is shown in Appendix A.2.

2.3.1 Correlated Photon Pair Source

The typical method of generating time-correlated photon pairs is to make use of the nonlinearity of optical material. Spontaneous parametric down conversion (SPDC) and four-wave mixing (FWM) [55] are the two commonly used methods to generate correlated photon pairs.

SPDC relies on the $\chi^{(2)}$ nonlinearity of a crystal where a photon from the pump light (frequency ω_3) is converted into two photons of lower energy (ω_1 and ω_2) observing the conservation of momentum (phase matching, $\Delta\vec{k} = \vec{k}_1 + \vec{k}_2 - \vec{k}_3 = 0$) and energy ($\omega_1 + \omega_2 = \omega_3$). The commonly used crystals are KD*P (potassium dideuterium phosphate), BBO (beta barium borate), etc., chosen according to the strength of the $\chi^{(2)}$ as well as the compatibility between pump wavelength and phase matching condition. High collection efficiency [56] as well as high generation efficiency using periodically-poled crystal [57] of the photon pairs have been demonstrated. In the context of interacting different physical systems in a quantum network, the drawback associated with these SPDC-based photon pairs sources is its large optical bandwidth ($\sim 100\,\text{GHz}$ to $2\,\text{THz}$), which is incompatible with the typical bandwidth of the optical transitions in atomic system ($\sim$ MHz). Recently a narrow-band ($\sim 10\,\text{MHz}$) source of SPDC-based photon pairs has been demonstrated with the help of whispering gallery mode resonator [58] or resonant cavities [59, 60].

Another approach uses FWM that relies on the $\chi^{(3)}$ nonlinearity of the optical medium to generate the photon pairs. It converts two pump photons (ω_1, ω_2) into two correlated photons (ω_i, ω_s) under the conservation of energy $(\omega_1 + \omega_2 = \omega_i + \omega_s)$ and phase matching $(\Delta\vec{k} = \vec{k}_1 + \vec{k}_2 - \vec{k}_i - \vec{k}_s = 0)$. FWM has been demonstrated in optical medium such as optical fiber [61, 62] as well as atomic vapour [26, 63, 64, 65]. The use of atomic vapour as the optical medium can be advantageous because the bandwidth of the photon pairs source can be made to be compatible with typical bandwidth in atomic system by using, for instance, the same species of atom. Generation of correlated photon pairs in warm atomic vapour suffers from wide bandwidth ($300 - 400\,\text{MHz}$) due to the Doppler broadening effect caused by the motion of atoms. However, this can be circumvented by using a cold atomic ensemble where the Doppler effect can be heavily suppressed. This has been demonstrated by [26, 63] where the generated photon pairs source has very narrow bandwidth ($\sim$ MHz).

2.3.2 Narrow Band Photon Pairs via Four-Wave Mixing in a Cold Atomic Ensemble

The setup presented in this section is almost identical to the one presented in [26] with a difference in the FWM transition. Fig. 2.13b shows the energy levels in ^{87}Rb that participate in the FWM process. Two pump beams at 795 nm and 762 nm excite the atomic ensemble from $|5S_{1/2}, F = 2\rangle$ to $|5D_{3/2}, F'' = 3\rangle$ through the two-photon transition. The 795 nm beam is 30 MHz red-detuned from the $|5P_{1/2}, F' = 2\rangle$ in order to minimize the incoherent scattering back to the ground state. The two possible decay paths from $|5D_{3/2}, F'' = 3\rangle$ to $|5P_{3/2}\rangle$ (solid line and dashed line in Fig. 2.13b) can lead to photon pairs that are entangled in frequency. By tuning the polarisation of the two pump beams and selecting only certain polarisation at each output, it is possible to obtain correlated photon pairs produced along one of the decay path only.

An ensemble of ^{87}Rb atoms is generated using MOT. Each MOT beam consists of a cooling beam 24 MHz red-detuned from the $|5S_{1/2}, F = 2\rangle \rightarrow |5P_{3/2}, F' = 3\rangle$ transition, and a repump beam tuned to $|5S_{1/2}, F = 1\rangle \rightarrow |5P_{3/2}, F' = 2\rangle$ transition. The power of each MOT cooling beam is ~40 mW and the MOT repump beam sums up to ~10 mW. These powers are much larger than the ones used in single atom setup (Section 2.2.2) as a larger number of atoms is required.

A schematic diagram of the experimental setup is shown in Fig. 2.13a. The two orthogonally polarised pump beams (H for 795 nm and V for 762 nm) are combined and sent in a collinear configuration to the atomic ensemble. By selecting horizontally-polarised signal photons and vertically-polarised idler photons, we can obtain photon pairs generated along $|5D_{3/2}, F'' = 3\rangle \rightarrow |5P_{3/2}, F' = 3\rangle \rightarrow |5S_{1/2}, F = 2\rangle$.

The experimental sequence for the generation of the correlated photon pair is shown in Fig. 2.13c. The MOT is switched on for 80 μs, followed by 10 μs of optical pumping. During the pumping stage, the detection gate to the timestamp module is also switched on. Fig. 2.14 shows the heralded 780 nm single photon ($|5P_{3/2}, F' = 3\rangle \rightarrow |5S_{1/2}, F = 2\rangle$) from time-correlated photon pair produced through FWM in a cold ^{87}Rb atomic ensemble. An exponential fit to the photon shape shows a characteristic decay time of 14.1 ns which smaller than the lifetime of $5P_{3/2}$ (27 ns). This is associated with the superradiance effect [66, 67] which is the cooperative decay effect exhibited by a collection of identical atoms that causes them to decay faster than the incoherent

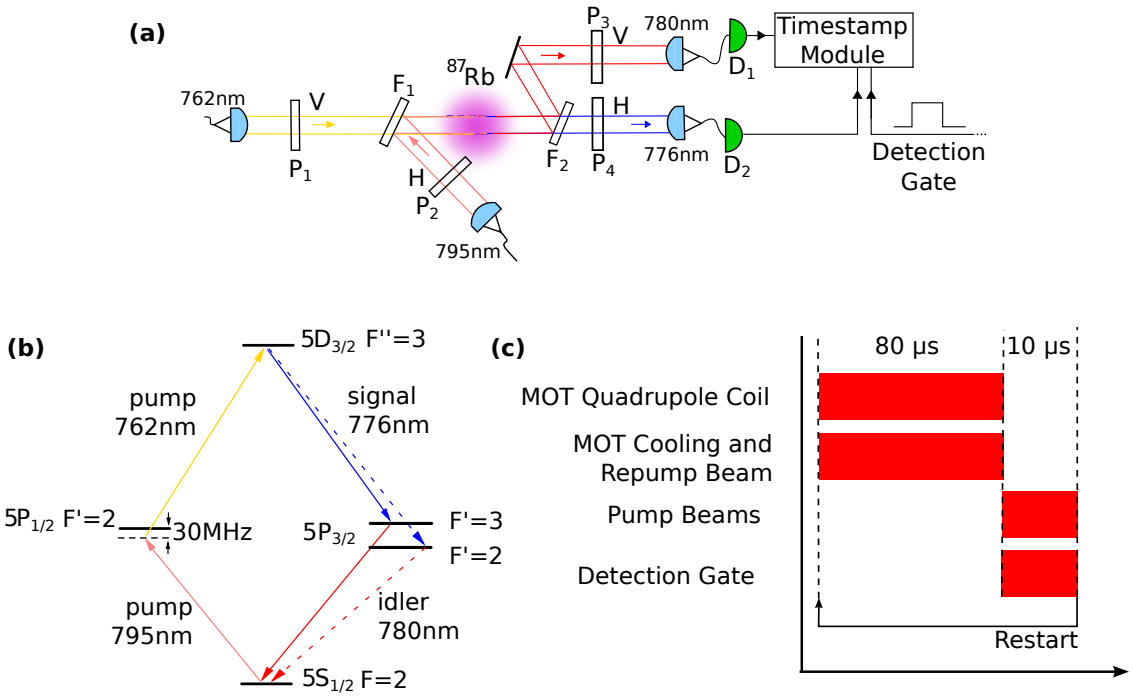

Figure 2.13: **(a)** Schematic diagram of the experimental setup for FWM in collinear configuration. P_1 and P_3 select the vertical polarisation (V) while P_2 and P_4 select the horizontal polarisation (H). F_1 and F_2: Interference filters. D_1 and D_2: Silicon Avalanche Photo-Diode. **(b)** ^{87}Rb level transitions in FWM. **(c)** Experimental sequence for the generation of the correlated photon pair.

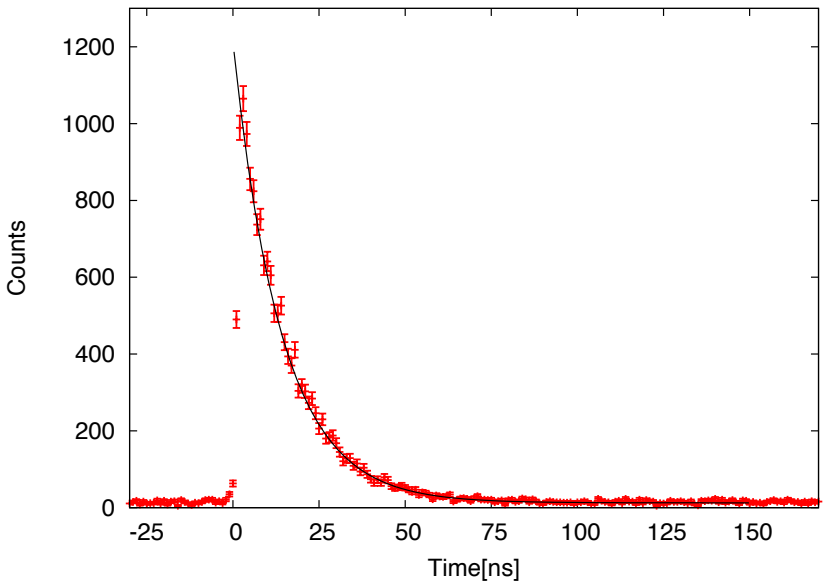

Figure 2.14: Heralded 780 nm single photon from the photon pair produced through four-wave mixing in a cold ^{87}Rb atomic ensemble. (Red data points) Recorded detection events in detector D_1 (refer to Fig. 2.13) with $t = 0$ corresponding to the detection in detector D_2. The displayed error bar is the standard deviation of each data point attributed to the Poissonian counting statistics. The black line is an exponential fit with a characteristic decay time of 14.1±0.2 ns. Data is processed in 1 ns timebin.

emission lifetime. This decay time can be varied by changing the density of the atomic cloud as shown in [26].

3

Two-Photon Interference Experiment

In this chapter, we present the two-photon interference experiment in which two single photons from two different sources interfere at a 50:50 beam splitter and show that we observed the Hong-Ou-Mandel dip. In the following, we refer to the single atom setup as the SA setup and the atomic ensemble setup as the FWM (four-wave mixing) setup. The same naming convention applies to their single photons as well.

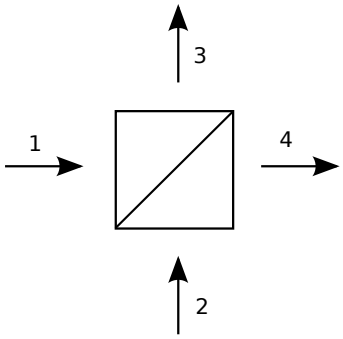

Figure 3.1: Beam splitter. The two input modes are labelled 1 and 2; output modes are labelled 3 and 4.

3.1 Introduction to the Hong-Ou-Mandel Interference

When two indistinguishable[1] single photons enter the inputs of a 50:50 beam splitter, the two photons always emerge together from either output of the beam splitter. In order to understand the origin of this effect, we first consider the case where the two single photons are in the same single frequency mode and share the same polarisations. In the Heisenberg picture, the creation operators of photons at the input modes of the beam splitter are labelled $\hat{a}_1^\dagger$ and $\hat{a}_2^\dagger$ and those of the output modes as $\hat{a}_3^\dagger$ and $\hat{a}_4^\dagger$ (refer to Fig. 3.1). For a lossless beam splitter, the output modes can be related to the input modes through the following relations [68]:

$$\hat{a}_1^\dagger = -r\,\hat{a}_3^\dagger + t\,\hat{a}_4^\dagger \qquad , \qquad \hat{a}_2^\dagger = t\,\hat{a}_3^\dagger + r\,\hat{a}_4^\dagger\,, \tag{3.1}$$

where r and t are real numbers and the minus sign ensures energy conservation ($r^2+t^2 = 1$). With one photon in each input mode, i.e. $|1_1, 1_2\rangle$, the beam splitter transforms it into

$$|1_1, 1_2\rangle = \hat{a}_1^\dagger \hat{a}_2^\dagger |0\rangle \longrightarrow \left(-r\,\hat{a}_3^\dagger + t\,\hat{a}_4^\dagger\right)\left(t\,\hat{a}_3^\dagger + r\,\hat{a}_4^\dagger\right)|0\rangle \tag{3.2}$$

$$= \left(-rt\,\hat{a}_3^\dagger \hat{a}_3^\dagger + rt\,\hat{a}_4^\dagger \hat{a}_4^\dagger - r^2\,\hat{a}_3^\dagger \hat{a}_4^\dagger + t^2\,\hat{a}_4^\dagger \hat{a}_3^\dagger\right)|0\rangle \tag{3.3}$$

$$= -\sqrt{2}rt|2_3, 0_4\rangle + \sqrt{2}rt|0_3, 2_4\rangle + (-r^2 + t^2)|1_3, 1_4\rangle \tag{3.4}$$

The $|2_3, 0_4\rangle$ and $|0_3, 2_4\rangle$ terms of expression (3.4) correspond to the two photons emerging together from either output of the beam splitter while the $|1_3, 1_4\rangle$ term corresponds to one photon emerging from different outputs of the beam splitter. As the two possible paths that lead to $|1_3, 1_4\rangle$ are indistinguishable, the probability amplitudes must be summed. For a 50:50 beam splitter, i.e. $r = t = \frac{1}{\sqrt{2}}$, the probability amplitudes for $|1_3, 1_4\rangle$ state interfere destructively. Consequently, the photons always emerge together from either output of the beam splitter. The first experimental demonstration of this phenomenon is by Hong, Ou and Mandel [11] in 1987. This phenomenon is referred to as the Hong-Ou-Mandel (HOM) interference, or two-photon interference.

The above argument assumes a single frequency radiation mode while in practice the single photon produced in laboratory has a finite bandwidth and is localised in space and time. To account for this, the problem is treated in the continuous-mode

[1]The indistinguishability refers to sharing the same spatial, temporal, frequency, polarisation modes.

operator formalism as demonstrated in [68, Chap. 6]. This treatment assumes that the photon bandwidth is sufficiently narrow such that the beam splitter response is approximately constant in the frequency range of the photon. We consider the special case where the single photon at input 1 is independent of the single photon at input 2 and label their wavepacket temporal amplitudes by $\xi_1(t)$ and $\xi_2(t)$, respectively[1]. Then the probability of finding one photon at each output of the beam splitter, $P(1_3, 1_4)$, as well as the probability of finding two photons at either output of the beam splitter, $P(2_3, 0_4)$ and $P(0_3, 2_4)$, are

$$P(1_3, 1_4) = 1 - 2r^2t^2 \left(1 + |J|^2\right) \tag{3.5}$$

$$P(2_3, 0_4) = P(0_3, 2_4) = r^2t^2 \left(1 + |J|^2\right) , \tag{3.6}$$

where $|J|^2$ is called the overlap integral defined as

$$|J|^2 = \left| A \int \xi_1(t)^* \, \xi_2(t) \, dt \right|^2 . \tag{3.7}$$

The $\left|\int \xi_1(t)^* \, \xi_2(t) \, dt\right|^2$ term represents the temporal overlap. The coefficient A represents the overlap in the other modes such as the spatial mode overlap between the two input modes at the beam splitter, input polarisations, etc. If there is a complete overlap between the two photons ($|J|^2 = 1$), then the two photons are indistinguishable.

For a 50:50 beam splitter and $|J|^2 = 1$, then $P(1_3, 1_4) = 0$ and the two photons always emerge together from same, yet random output. If the two single photons have different bandwidths, then $P(1_3, 1_4)$ does not vanish as the temporal overlap is never perfect, i.e. $\left|\int \xi_1(t)^* \, \xi_2(t) \, dt\right|^2 \neq 1$. If the two photons have orthogonal polarisations, then $A = 0$ even for a complete temporal overlap between the two input photons, and consequently there is no HOM interference as the two photons can be distinguished from each other. In this non-interfering case, the beam splitter acts on the photon at one input independent of the photon at the other input.

3.2 Joint Experimental Setup

Fig. 3.2 illustrates the joint experimental setup of the single atom (SA) setup, atomic ensemble or four-wave mixing (FWM) setup, and the Hong-Ou-Mandel (HOM) interferometer.

[1] The amplitude is normalised to 1, i.e. $\int |\xi(t)|^2 \, dt = 1$

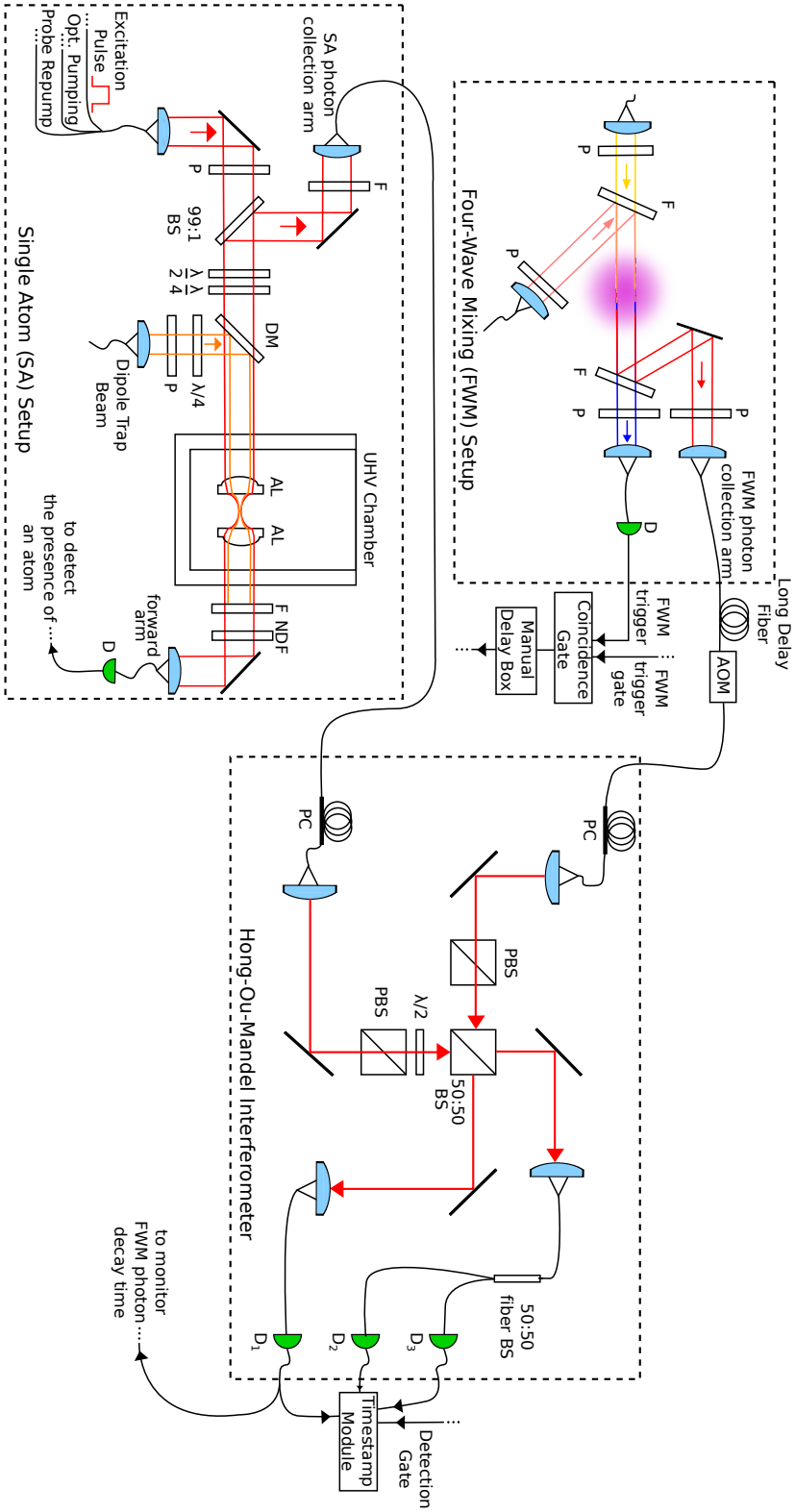

Figure 3.2: Joint setup of the single atom (SA) setup and the atomic ensemble or four-wave mixing (FWM) setup for the two-photon interference experiment. P: polariser. F: interference filters. D, D_1, D_2, D_3: silicon avalanche photodiodes. DM: dichroic mirror. AL: aspheric lens. UHV chamber: ultra high vacuum chamber. PC: fiber polarisation controller. $\lambda/2$: half-wave plate. $\lambda/4$: quarter-wave plate. PBS: polarising beam splitter. BS: beam splitter. The manual delay box is used to vary the time delay between the two single photons by delaying the arrival of the FWM trigger at the SA setup. For more information, refer to Section 2.2.4.2 for the SA setup and Section 2.3.2 for the FWM setup.

3.2.1 The Mach-Zehnder Interferometer

In order to observe the HOM interference, it is necessary that the two input spatial modes overlap at the beam splitter. A Mach-Zehnder interferometer is constructed around the HOM interferometer to verify this overlap as shown in Fig. 3.3. A fiber beam splitter splits a laser beam into two paths. An optical path difference of a few cm is introduced by adding a free-space coupling link. The beam splitter in the HOM interferometer acts as the second beam splitter in the Mach-Zehnder interferometer.

The two input beams are tuned to have equal power and parallel polarisations at the beam splitter of the HOM interferometer. Fig. 3.4 shows the temporal fluctuation of the photodetector signal measured at one of the outputs. The passive instability of the free-space link is enough to introduce variation in the optical path difference between the two paths that changes the signal at the interferometer outputs. This passive instability is essentially captured by the irregular pattern of interference fringes shown in Fig. 3.4. Assuming that the photodetector response is linear in the signal range, the visibility of the interference, defined as

$$V = \frac{I_{max} - I_{min}}{I_{max} + I_{min}}, \tag{3.8}$$

is 98.1±1.5%, where I_{max} and I_{min} denote the maximum and minimum measured photodetector signal respectively. This signifies a good spatial overlap between the two input beams at the beam splitter.

3.2.2 Compensating for the Frequency Difference between the Single Photons

The frequency difference between the FWM and SA photons is largely attributed to the AC Stark effect due to the optical dipole trap and Zeeman effect due to the bias magnetic field. Both effects shift the energy levels of the single atom and in turn change the optical frequency of the SA photon. To compensate for this, the FWM photon passes through an acousto-optic modulator (AOM) before entering the HOM interferometer. The AOM increases the FWM photon optical frequency in order to match the optical frequency of the SA photon[1].

[1]Refer to Section 2.2.3 for the measurement of the resonance frequency of the two-level cycling transition in the ^{87}Rb used to produce the SA photon.

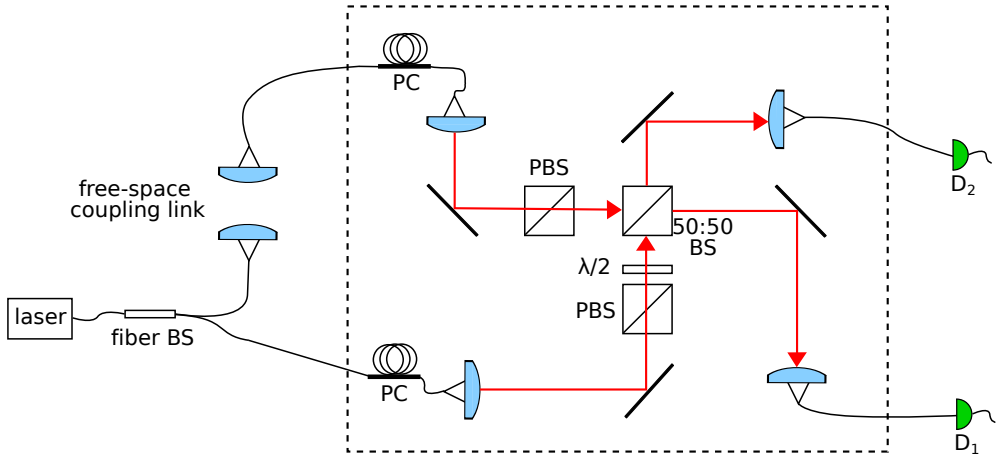

Figure 3.3: The Mach-Zehnder interferometer. The fiber polarisation controllers (PC) are set to maximise the transmission through the two polarising beam splitters (PBS). The two PBSs fix the polarisation of the two input beams. Depending on the orientation of the half-wave plate ($\lambda/2$), the two input beams can be made to interfere (parallel polarisation) or not (perpendicular polarisation) at the beam splitter (BS). $D_{1,2}$: photodetectors. The optical components inside the dashed rectangle is identical to the HOM interferometer used in the two-photon interference experiment.

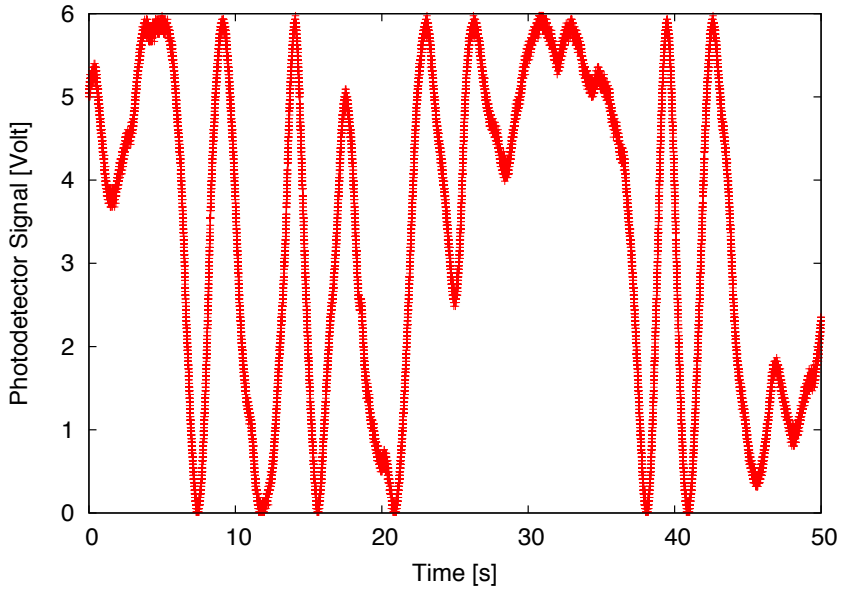

Figure 3.4: Photodetector signal measured at one of the outputs of the Mach-Zehnder interferometer. The variation in the Mach-Zehnder signal is caused by the passive instability of the optical path length in the free-space coupling link (Fig. 3.3). The measured visibility is 98.1±1.5%.

3.2.3 Decay Time Monitoring

While the decay time of the SA photon is fixed by the natural lifetime of the $5P_{3/2}$ of the single atom, the decay time of the FWM photon depends on the density of the atomic cloud which can fluctuate over time. It is therefore important to monitor and maintain the FWM photon's decay time (or equivalently the average density of the atomic cloud) during the two-photon interference experiment. Its decay time is monitored using one of the single photon detector (D_1) at one of the outputs of the HOM interferometer when there is no atom in the trap. During this time, the only photons from the SA setup reaching the HOM interferometer are those of the MOT fluorescence, which are uncorrelated with the FWM trigger. Thus measuring the detection events in D_1 conditional on the detection of the FWM trigger allows us to monitor the decay time of the FWM photon during the experiment.

3.3 Preparing the Single Atom Setup

In this section, we will discuss the work carried out on the single atom (SA) setup prior to the two-photon interference experiment.

3.3.1 Excitation Pulse Back-Reflection

In the previous pulsed excitation experiment (Section 2.2.4), the backward arm (or equivalently, the SA photon collection arm in Fig. 3.2) is used to detect the atomic fluorescence during the atom loading stage as well as to detect the single photon emission after each pulsed excitation. A strong neutral density filter (NDF, attenuation: 37 dB) is placed in the forward arm (Fig. 3.2) so as to not saturate the forward detector during the measurement of the optical pulse amplitude. The atomic fluorescence during the atom loading stage is thus highly attenuated in the forward arm, and cannot be used to check for the presence of an atom during the atom loading stage.

For the two-photon interference experiment, however, we only want to collect the SA photon from the SA photon collection arm and send it to the HOM interferometer. In principle, the detectors in the HOM interferometer can be used to detect the atomic fluorescence during the atom loading stage. However, the fluorescence signal would be too small by the time it reaches the detectors of the HOM interferometer due to the loss incurred along the way. As a consequence, we have to remove the strong NDF in

the forward arm and rely on the forward detector to detect the presence of single atom in the trap.

We first perform a measurement with the backward detector where we send a train of excitation pulses without an atom in the trap. We observe an increased background count rate, possibly due to the scattering of the excitation pulse picked up by the backward detector as shown in Fig. 3.5 (Legend: Configuration 1). There is also a strong back-reflection of the excitation pulse between 485 and 510 ns. These features will contaminate the single photon emission signal collected into the the SA photon collection arm.

To solve this, a 1.6 dB NDF is placed in the forward arm to suppress the increased background count rate while still allowing enough atomic fluorescence to be detected by the forward detector during atom loading stage. Furthermore, we extended the optical fiber between the collection lens and the forward detector in order to delay the back-reflection even further. The result is shown in Fig. 3.5 (Legend: Configuration 2). In this configuration, the back-reflection is pushed to approximately 87 ns from the beginning of the spontaneous emission This implies that approximately $1 - \exp(-87/27) = 96\%$ of the single photon emission is contained within the 87 ns window.

3.3.2 Optimum Excitation Period

We expect the following sequence during the two-photon interference experiment: after an atom is loaded into the optical dipole trap and prepared in the initial state of the two-level cycling transition, the atom is ready for excitation. During this excitation period, each arrival of the FWM trigger, that heralds the generation of a FWM single photon, automatically triggers the excitation of the single atom. The excitation period lasts for a time duration t_e. After the excitation period, the system will check for the presence of an atom in the trap and performs all the necessary steps until the next excitation period[1].

To maximise the duty cycle of the two-photon interference experiment, we would want t_e to be as long as possible. In principle, we should be able to extend t_e to the

[1] In the context of the previous pulsed excitation experiment presented in Section 2.2.4 (Fig. 2.10), the duration of the excitation period is $t_e = 1$ ms. In that experiment, the electrical trigger that leads to the excitation of the single atom is generated by the pattern generator.

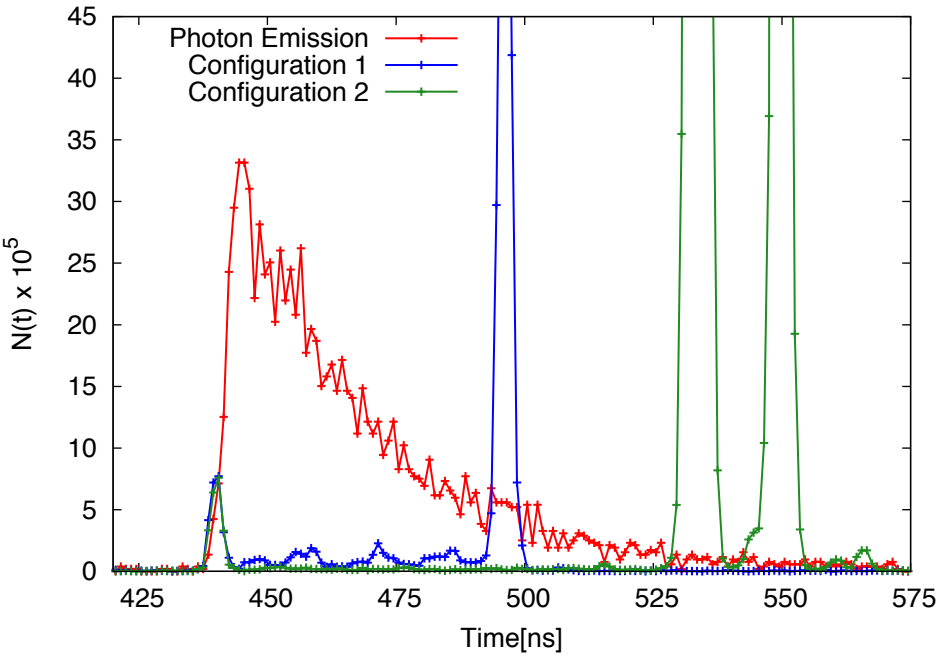

Figure 3.5: The vertical axis represents the normalised counts as defined in (2.1). (Photon Emission) The single photon emission from a single atom when a 37 dB attenuation neutral density filter (NDF) is used in the forward arm. (Configuration 1) The detection events in the backward detector when there is no NDF in the forward arm and no atom in the trap. There is an increased background count rate that can contaminate the single photon emission. The strong back-reflection between 485 and 510 ns originates from the optical fiber end in the forward arm. In this configuration, the optical fiber in the forward arm is left open-ended, i.e. not connected to the detector. (Configuration 2) The detection events in the backward detector with a 1.6 dB NDF used in the forward arm and no atom in the trap. The background count rate is suppressed. The strong back-reflection is pushed further in time by using a longer optical fiber in the forward arm. The back-reflection between 525 and 538 ns comes from the optical fiber end. The back-reflection between 538 and 560 ns comes from the surface of the detector. The signal between 435 and 440 ns for both Configuration 1 and 2, are similar to the one observed in Fig. 2.11. All data are processed in 1 ns timebins.

lifetime of the atom in the trap (~ 1 s). We will verify this with a series of measurements using the experimental sequence shown in Fig. 3.6. This sequence is similar to the one used during the pulsed excitation experiment (Section 2.2.4, Fig. 2.10), but instead of sending a fixed number of pulses at a fixed interval, each pulse is now triggered by the arrival of the FWM trigger at the SA setup. The FWM trigger rate is approximately $700\,\mathrm{s}^{-1}$, and simulates the condition of the actual two-photon interference experiment. The arrival of the FWM trigger will also open a detection gate that allows the timestamp module to record the detection events from the detectors for $2\,\mu$s. The experimental setup is similar to the setup used in the pulsed excitation experiment (Section 2.2.4, Fig. 2.8).

We are interested in the survival probability of the atom in the trap and the excitation probability. Both parameters have to be considered when choosing the optimal t_e. Any detection event that does not originate from the atom will decrease the signal to noise ratio. Also, the probability of having the SA photon and the FWM photon together in the HOM interferometer given there is a FWM trigger is very small, estimated to be[1] $\sim 3 \times 10^{-4}$. It is therefore important to maintain a high excitation probability of the SA during the excitation period to maximise the number of events in which the SA and FWM photons are together in the HOM interferometer.

It turns out that for an excitation period longer than a few milliseconds, the atom gets kicked out of the optical dipole trap due to the heating caused by resonant probe light that leaks through the two EOMs, even when there is no optical pulse being generated (refer to Section 2.2.4.1). To solve this, instead of leaving the probe AOM on constantly, functioning only as a frequency tuner of the probe light, we turn the AOM on only in a 200 ns time window in the vicinity of the excitation pulse. The switching on and off of the probe AOM improves the overall extinction ratio by > 40 dB when the excitation pulses are not being generated[2].

[1] The probability of having one SA photon in the HOM interferometer given there is a FWM trigger is calculated by summing the number of counts in detector D_1 (Fig. 3.2) within a time window, and dividing it with the number of FWM triggers and an efficiency factor. The time window is where the SA photon is expected to cause a detection event in the detector. The efficiency factor is the product of the fiber coupling efficiency (~ 0.7), the detection efficiency (~ 0.5), and the splitting ratio of the beam splitter (0.5). The same method is used to calculate the probability of having one FWM photon in the interferometer given there is a FWM trigger. The quoted value above is just the product of these two probabilities.

[2] Operating the probe AOM in this "pulsing" mode imposes a lower bound on the length of optical

We define the survival probability of the atom in the trap as

$$\text{Survival Probability} = \frac{\text{No. of survived cycles}}{\text{No. of new cycles}} \tag{3.9}$$

Fig. 3.7 shows the measurement of the survival probability and the excitation probability as the t_e is increased from 250 ms to 1500 ms. The decrease in the survival probability can be associated with an increase in the number of excitation cycles the atom undergoes, which causes it to heat up and escape from the dipole trap. The decrease in the excitation probability indicates that there is a limited number of excitation cycles the atom can go through before it exits the cycling transition (refer to Section 2.2.3.1). This may be caused by an impure σ_- polarisation of the excitation pulse that has an appreciable effect for large number of excitation cycles and long excitation period. From this measurement, we conclude that any t_e in between 250 and 500 ms is a reasonable choice while still maintaining high survival and excitation probability.

3.4 Experimental Sequence

The FWM and SA setups are operated independently. Fig. 2.13c and Fig. 3.8 show the experimental sequences operating on the FWM and the SA setups, respectively[1].

On the SA setup, once an atom in loaded into the optical dipole trap, the system performs molasses cooling to the atom to further cool it. From the result presented in Section 3.3.2, we decided to use a total excitation period of 500 ms duration, interspersed with 10 ms of state preparation every 100 ms. Then the system checks for the presence of an atom. If there is an atom, it returns to the molasses cooling stage. Otherwise, the system waits for the next atom to load into the trap.

The series of state preparation spread across the excitation period is to ensure that the atom always stays in the ground state of the cycling transition when it is waiting for the FWM trigger. The FWM trigger gate is an electronic gate that only activates during the excitation period. It allows the FWM triggers to reach the SA setup and subsequently trigger the excitation of the atom.

fiber that transports the FWM photon from the FWM setup to the HOM interferometer. For more information refer to Appendix C.1.

[1]For more information on Fig. 2.13c, refer to Section 2.3.2.

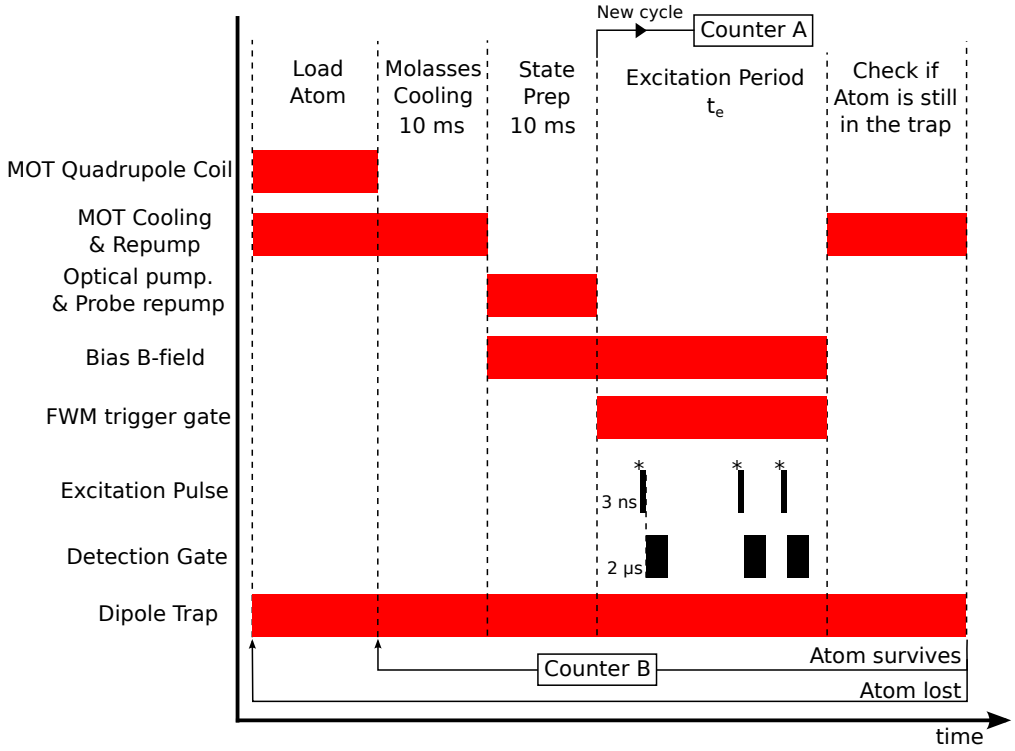

Figure 3.6: Experimental sequence for the measurement of the atom's lifetime in the dipole trap. Red colour signifies that it is controlled by the pattern generator. Black colour signifies that it is activated upon the arrival of the FWM trigger (Label:∗). Counters A and B record the number of new cycles and the number of cycles survived, respectively.

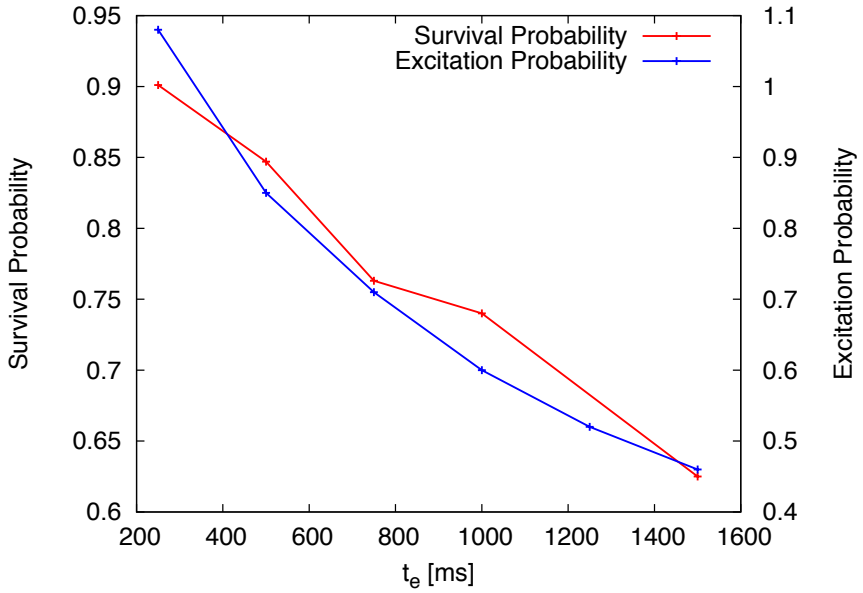

Figure 3.7: Measurement of survival probability and the excitation probability as a function of t_e. The survival probability is defined in (3.9). The excitation probability is defined in (2.2) assuming $\eta_d \cdot \eta_s \approx 0.01$ (refer to Section 2.2.4.3). The excitation probability goes above 1 for the t_e = 250 ms datapoint due to the assumption that the quantum efficiency of the detector, η_d, is equal to 0.5.

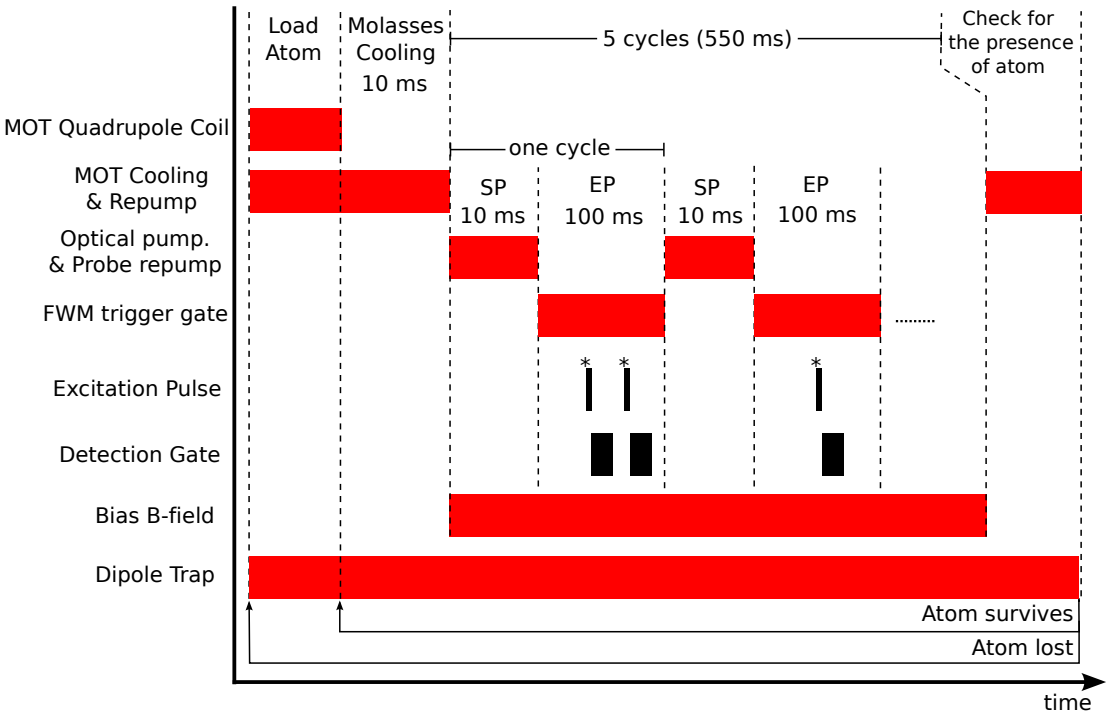

Figure 3.8: Experimental sequence of the SA setup during the two-photon interference experiment. SP: state preparation of atom ($|5S_{1/2}, F = 2, m_F = -2\rangle$). EP: excitation period during which an incoming FWM trigger (Label:$*$) will lead to the creation of a 3 ns excitation pulse that excites the atom and open a detection gate that allows the timestamp module to record the detectors counts for 2 μs.

3.5 Interfering the Two Single Photons

To analyse the results of the two-photon interference experiment, we look at the coincidence measurements between the FWM triggers[1] and the clicks in the three detectors within an 80 ns coincidence window[2].

We denote the FWM trigger as 0 and the detectors D_1, D_2, D_3 of the HOM interferometer as 1, 2 and 3, respectively. For instance, N_{012} denotes the number of three-fold coincidences between the FWM trigger, and a click in both detector D_1 and D_2 within the 80 ns coincidence window. The same naming convention applies to N_{013} and N_{023}. In this notation, $N_{012} + N_{013}$ is proportional to $P(1_3, 1_4)$ (refer to Section 3.1) and N_{023} is proportional to $P(2_3, 0_4)$ with proportionality constants that depend on the detection efficiencies, beam splitter splitting ratios, number of FWM triggers, etc.

Apart from the three-fold coincidence events between the FWM trigger, SA photon and FWM photon, these measured values also include the accidental coincidences, denoted as A_{012}, A_{013}, and A_{023}. They are associated with the detection of either SA or FWM photon in one of the detector and an accidental click (due to background noise, dark counts, etc.) in the other, as well as accidental coincidence events due to accidental clicks in both detectors. The estimation of the accidental coincidences is discussed in Appendix C.2.

3.5.1 Effect of Time Delay between the Single Photons

In the first experiment, the SA photon and FWM photon are set to have parallel polarisations. The decay time of the FWM photon is maintained at 14 ± 1 ns. We measure the three-fold coincidences between the FWM trigger and any two of the three detectors of the HOM interferometer (D_1, D_2, D_3) as a function of the time delay between the two single photons, Δt_p. The arrival time of the FWM photon is fixed with respect to the FWM trigger, while the arrival time of the SA photon is varied by changing the time at which the atom is excited. The time delay Δt_p between the two photons is defined as the time difference between the beginning of the exponential decay

[1] The FWM triggers here are only those that arrive at the SA setup.

[2] The coincidence window is the time window within which we expect to see detections originating from the two single photons that have interfered.

of each photon's wave packet amplitude reconstructed in the single photon detector with a resolution limited by the resolution of the detector (1 ns).

A positive Δt_p corresponds to the FWM photon arriving earlier than the SA photon. We define the total number of the FWM trigger that arrives at the SA setup as N_0. The quantities C and C' are the normalised coincidences between the two outputs of the beam splitter without and with accidentals correction, respectively. They are defined as

$$C = \frac{N_{012} + N_{013}}{N_0}\,, \tag{3.10}$$

$$C' = \frac{N_{012} + N_{013} - A_{012} - A_{013}}{N_0}\,. \tag{3.11}$$

The results are shown in Fig. 3.9.

As the temporal overlap between the two single photons is maximal when the two photons arrive at the same time on the beam splitter, this should result in the lowest $P(1_3, 1_4)$ as predicted by (3.5). This agrees well with the results in Fig. 3.9, where the measured coincidences between the two outputs of the beam splitter in the $\parallel$ polarisations case are the lowest when the two photons arrive at the same time on the beam splitter (Δt_p =0 ns). This is what is usually referred to as the HOM dip. As the time difference between the arrivals of the two photons, $|\Delta t_p|$, increases, the measured coincidences become larger and tend towards the non-interfering case ($\perp$ polarisations). This is expected in the limit of large $|\Delta t_p|$, where the beam splitter acts on the photon in one input independently of the other photon of the other input.

Fig. 3.9 also shows the theoretical curves, obtained from $P(1_3, 1_4)$ of (3.5) for different Δt_p, for both corrected and uncorrected cases. The asymmetry of the curves with respect to $\Delta t_p = 0$ ns is due to the unequal bandwidths or decay times of the two photons that causes the overlap integral (3.7) to be asymmetric with respect to the origin[1]. The constant A that represents the overlap in modes other than the temporal overlap between the two photons[2] is lower for the uncorrected case as it also takes into account the accidentals that diminish the interference effect.

[1] If the two photons have the same decay time or bandwidth, then the overlap integral would be symmetrical about $\Delta t_p = 0$ ns and the curves would be symmetrical too.

[2] Refer to (3.7) in Section 3.1

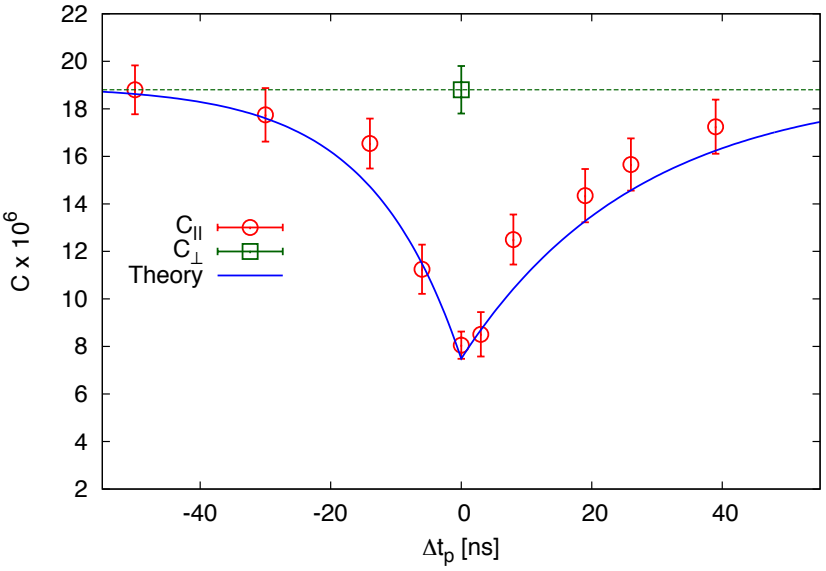

(a) Raw coincidence measurement

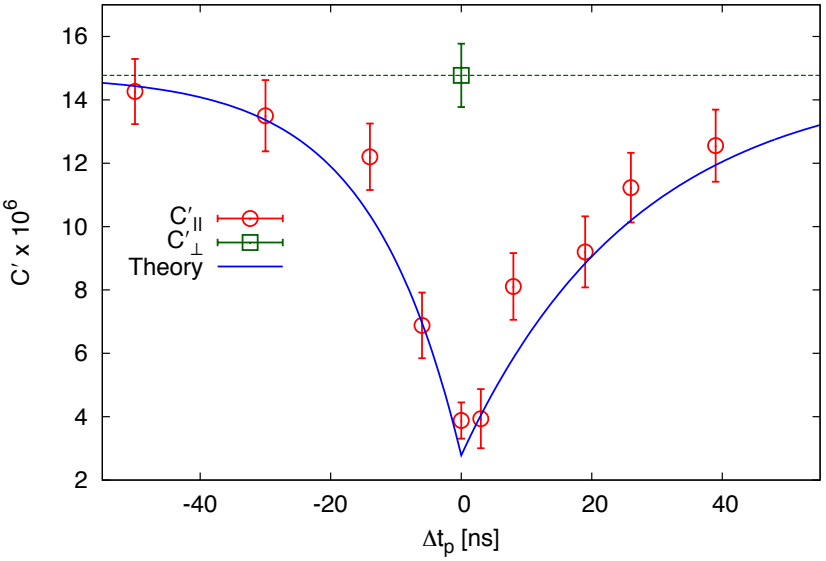

(b) Coincidence measurement corrected for the accidentals

Figure 3.9: Normalised coincidence measurements between the two outputs of the beam splitter, C and C' defined in (3.10) and (3.11) respectively, as a function of the time delay between the two single photons Δt_p. The circles and squares correspond to the two single photons having $\parallel$ or $\perp$ polarisations, respectively. The solid line represents the theoretical curve calculated using $P(1_3, 1_4)$ in (3.5) for two exponentially decaying wavepackets with decay times of 14 ns (FWM) and 27 ns (SA), assuming a 50:50 beam splitter. The theoretical curve for (a) and (b) corresponds $A = 0.82$ and $A = 0.95$, respectively. Each theoretical curve is normalised such that it approaches the value of C (or C') obtained for the $\perp$ case in the limit of large $|\Delta t_p|$. The error bars reflect Poissonian statistical uncertainties.

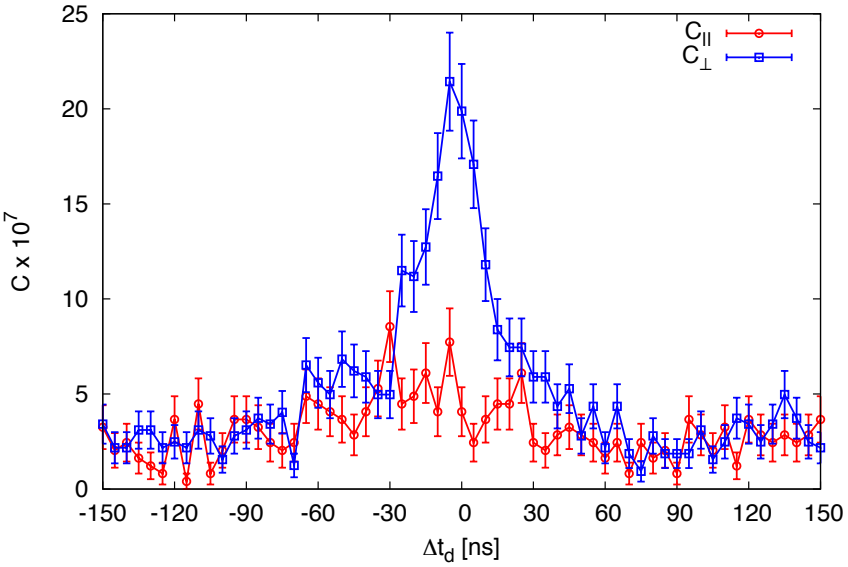

Figure 3.10: Conditional second order correlation measurement between the two outputs of the beam splitter, i.e. between clicks in detector D_1 and detectors $\{D_2,D_3\}$, conditioned on the presence of a FWM trigger for $\Delta t_p = 0$. Δt_d is the delay between the detections at the the two outputs. The data is processed in 5 ns time bins. Circles and squares correspond to the case of $\parallel$ and $\perp$ polarisations respectively.

The HOM interference visibility is defined as the depth of the observed HOM dip at $\Delta t_p = 0$ ns:

$$V_1 = \left(1 - \frac{C_{\parallel}}{C_{\perp}}\right)\Bigg|_{\Delta t_p=0}, \tag{3.12}$$

where $C_{\parallel}$ and $C_{\perp}$ correspond to the parallel and perpendicular cases, respectively. The measured visibility is 57±3% before correction and 74±3% after correction.

Another method used to quantify the interference visibility is based on the second-order correlation measurement between the two outputs of the beam splitter for $\Delta t_p = 0$ as a function of the delay between the detection events Δt_d at the two beam splitter outputs, conditional on the FWM trigger. Fig. 3.10 shows the result for both the interfering ($\parallel$ polarisations) and non-interfering case ($\perp$ polarisations). The result is not corrected for accidentals.

For the non-interfering case, there is a large increase in the coincidences between the two outputs for small $|\Delta t_d|$ values (of the same order of magnitude as the decay time

of the single photons, i.e. 14 ns (FWM) and 27 ns (SA)) as compared to the interfering case. For larger $|\Delta t_d|$, the coincidences for both cases level off to the same level, which can be attributed to the background counts. Following the definition in [24], the HOM interference visibility is defined as

$$V_2 = 1 - \frac{\int_{-T}^{T} C_{\parallel}(\tau)\, d\tau}{\int_{-T}^{T} C_{\perp}(\tau)\, d\tau}, \tag{3.13}$$

where $\tau = \Delta t_d$ and T is the range of integration. For $T = 30$ ns, we obtained $V_2 = 61 \pm 4\%$ that is in agreement with the visibility value obtained previously through (3.12) for the uncorrected case (57±3%). This visibility value is an improvement with respect to the $16 \pm 3\%$ visibility reported by Polyakov et al [24] (PDC and quantum dot)[1] and comparable to the 70% visibility reported by McMillan et al [25] (PPLN waveguide and microsctructured fiber). Note that our result is obtained without any need for spectral filtering as the two single photons are already bandwidth-compatible. A higher visibility can be achieved by using a smaller range of integration. The visibility V_2 starts to decrease for larger T due to the background counts.

3.5.2 Effect of FWM Photon Decay Time

We also examined the HOM interference effect for different decay times of the FWM photon. Different decay times are obtained by changing the average density of the atomic cloud. This would lead to different photon pair production efficiencies for different decay times. The pair production efficiency refers to the number of FWM photons produced divided by the number of FWM triggers. It is therefore not possible to directly compare the normalised coincidences C and C', as defined in (3.10) and (3.11), for different decay times.

In the following, we consider the ratio between the coincidences of the two beam splitter outputs (N_{012}+N_{013}) and the coincidences within the same beam splitter output (N_{023}):

$$\beta = \frac{N_{012} + N_{013}}{N_{023}}. \tag{3.14}$$

This quantity β is independent of the photon-pair production efficiency, making it possible to compare the values of β obtained for different FWM photon decay time.

[1] Polyakov et al. [24] used the same definition as (3.13) and referred to it as the "two-photon coalescence probability".

It is proportional to $\frac{P(1_3,1_4)}{P(2_3,0_4)}$ with a proportionality constant that depends only on the splitting ratio of the beam splitters and the detection efficiencies[1].

By dividing the measurement of β for the $\parallel$ polarisations ($\beta_{\parallel}$) with the one for $\perp$ polarisations ($\beta_{\perp}$), we obtain a ratio ($\frac{\beta_{\parallel}}{\beta_{\perp}}$) which is independent of this proportionality constant and can also be calculated from $\frac{P(1_3,1_4)}{2P(2_3,0_4)}$ using (3.5) and (3.6) assuming a 50:50 beam splitter[2]. HOM interference corresponds to $\frac{\beta_{\parallel}}{\beta_{\perp}} < 1$. In principle, if the two photons are completely indistinguishable, we should measure $\frac{\beta_{\parallel}}{\beta_{\perp}} = 0$.

The quantity $\beta_{\perp}$ can be calculated by directly measuring the three-fold coincidences, i.e. $N_{012}, N_{013}, N_{023}$, with photons of $\perp$ polarisations. Alternatively, one can also make use of the fact that in the $\perp$ case where the two input photons do not interfere, the counts in the three detectors are independent of each other. Therefore[3]

$$\beta_{\perp} = \frac{(N_{012,\perp} + N_{013,\perp})}{N_{023,\perp}} \tag{3.15}$$

$$= \frac{N_{01,\perp}(N_{02,\perp} + N_{03,\perp})}{N_{02,\perp}N_{03,\perp}}. \tag{3.16}$$

Instead of repeating the measurements for the $\perp$ case, we simply note that the number of two-fold coincidences in the measurement with $\parallel$ polarisations is ~4 orders of magnitude greater than the number of three-fold coincidences. This is due to the fact that the probability of having the SA photon and the FWM photon together in the HOM interferometer is very small. Therefore most of the time, there is only one single photon, either from SA or FWM setup, in the HOM interferometer. Therefore for large number of FWM triggers,

$$\beta_{\perp} \approx \frac{N_{01,\parallel}(N_{02,\parallel} + N_{03,\parallel})}{N_{02,\parallel}N_{03,\parallel}}, \tag{3.17}$$

with the actual HOM interference contributing a tiny error to each of the two-fold coincidences.

Fig. 3.11 shows the measured $\beta_{\parallel}/\beta_{\perp}$ (corrected for accidentals) as a function of the FWM photon decay time. The measured result shows a behaviour that is consistent with the theory, i.e. a greater difference in the decay time of both photons corresponds

[1] The detection efficiencies include the quantum efficiencies of the detectors and other losses in the HOM interferometer.

[2] $\frac{\beta_{\parallel}}{\beta_{\perp}} = \left(\frac{P(1_3,1_4)}{P(2_3,0_4)}\right)_{\parallel} / \left(\frac{P(1_3,1_4)}{P(2_3,0_4)}\right)_{\perp}$ with $\left(\frac{P(1_3,1_4)}{P(2_3,0_4)}\right)_{\perp} = 2$ in the case of a 50:50 beam splitter.

[3] Refer to Appendix C.3 for more information.

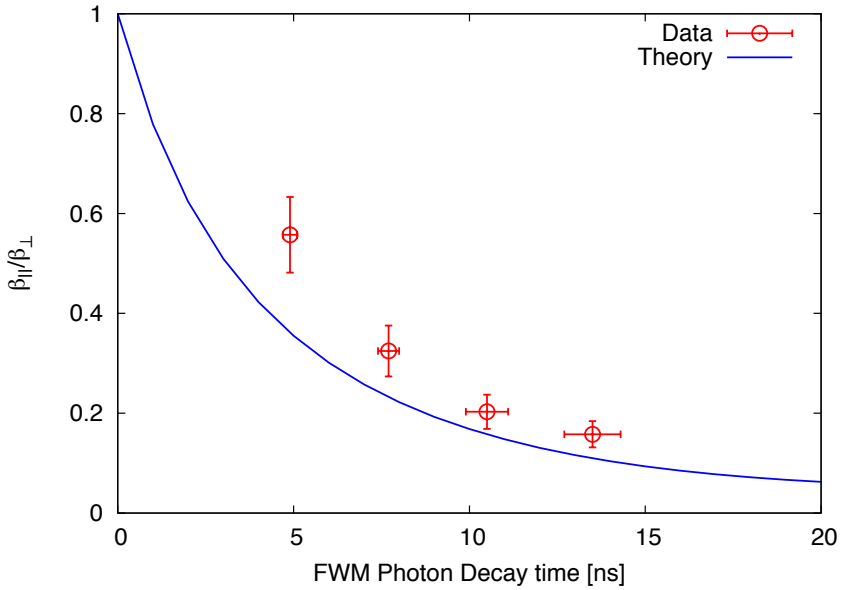

Figure 3.11: Plot of the ratio of β, as defined in (3.14), between the $\|$ and $\perp$ case for different FWM photon decay times. The theory curve is obtained from $\frac{P(1_3,1_4)}{2P(2_3,0_4)}$ in (3.5) and (3.6) for $\Delta t_p = 0\,\text{ns}$ and $A = 0.95$. Recall that the decay time of the SA photon is $\approx 27\,\text{ns}$.

to a smaller temporal overlap between the two photons that, in turn, diminishes the HOM interference effect. As a result, the ratio $\frac{\beta_{\|}}{\beta_{\perp}}$ approaches 1 (non-interfering case) as the FWM photon decay time decreases.

3.6 Conclusion & Outlook

We have demonstrated the HOM interference between two single photons produced by two different physical systems: a single atom and a cold atomic ensemble. The behaviour of the HOM interference is examined for different time delays between the two photons and also for different photon bandwidths. The measured interference visibility (57±3% without any accidental correction) is an improvement with respect to the one reported by [24] and comparable to the one reported by [25]. This result, however, is obtained without any need for spectral filtering as the two photons produced by our systems are already compatible in bandwidth. Our results demonstrate the importance of manipulating coherently the photons produced by different physical systems in order to match the photon bandwidths to achieve high HOM interference visibility. This also opens up an avenue to demonstrate the entanglement between a single atom and a cold atomic ensemble that relies on this interference effect [69]. This entanglement scheme does not require any direct interaction between the two physical system.

In the quest for efficient atom-light interaction, we also plan to send a single photon with an exponentially rising profile to the single atom and show that it is possible to achieve high excitation efficiency. Similar work has been done before, in the same single atom setup, but with a coherent optical pulse of exponentially rising profile. It was shown to achieve a more efficient excitation as compared to the excitation with a coherent optical pulse of square envelope. The ability to generate a single photon with an exponentially rising profile from a cold atomic ensemble has been demonstrated by [70].

References

[1] Kok, P., Nemoto, K., Ralph, T. C., Dowling, J. P. & Milburn, G. J. Linear optical quantum computing with photonic qubits. *Reviews of Modern Physics* **79**, 135–174 (2007). URL `http://link.aps.org/doi/10.1103/RevModPhys.79.135`. 1

[2] Gisin, N. & Thew, R. Quantum Communication. *Nature Photonics* 165–171 (2007). 1

[3] Shor, P. W. Polynomial-Time Algorithms for Prime Factorization and Discrete Logarithms on a Quantum Computer 28 (1995). URL `http://arxiv.org/abs/quant-ph/9508027`. `9508027`. 1

[4] Kimble, H. J. The Quantum Internet. *Nature* **453**, 1023–30 (2008). URL `http://www.ncbi.nlm.nih.gov/pubmed/18563153`. 1

[5] Wineland, D. J. *et al.* Quantum information processing with trapped ions. *Philosophical transactions. Series A, Mathematical, physical, and engineering sciences* **361**, 1349–61 (2003). URL `http://www.ncbi.nlm.nih.gov/pubmed/12869312`. 1

[6] Enk, S. V., Kimble, H. & Mabuchi, H. Quantum information processing in cavity-QED. *Experimental Aspects of Quantum ...* **3**, 75–90 (2005). URL `http://link.springer.com/chapter/10.1007/0-387-27732-3_6`. 1

[7] Jessen, P. & Stock, R. Quantum information processing with trapped neutral atoms. *Quantum Information Processing* **3**, 91–103 (2004). URL `http://link.springer.com/article/10.1007/s11128-004-9418-2`. 1

[8] Wrachtrup, J. & Jelezko, F. Processing quantum information in diamond. *Journal of Physics: Condensed Matter* **18**, S807–S824 (2006).

URL http://stacks.iop.org/0953-8984/18/i=21/a=S08?key=crossref.3ebf978682f06b8bfab48217febea4e1. 1

[9] Imamoglu, A. *et al.* Quantum information processing using quantum dot spins and cavity QED. *Physical Review Letters* **83**, 4204–4207 (1999). URL http://journals.aps.org/prl/abstract/10.1103/PhysRevLett.83.4204. 1

[10] Knill, E., Laflamme, R. & Milburn, G. J. A scheme for efficient quantum computation with linear optics. *Nature* **409**, 46–52 (2001). URL http://www.ncbi.nlm.nih.gov/pubmed/11343107. 2, 4

[11] Hong, C., Ou, Z. & Mandel, L. Measurement of subpicosecond time intervals between two photons by interference. *Physical Review Letters* (1987). URL http://www.inoa.it/home/azavatta/References/PRL59p2044.pdf. 2, 30

[12] Riedmatten, H., Marcikic, I., Tittel, W., Zbinden, H. & Gisin, N. Quantum interference with photon pairs created in spatially separated sources. *Physical Review A* **67**, 022301 (2003). URL http://link.aps.org/doi/10.1103/PhysRevA.67.022301. 2

[13] Kaltenbaek, R., Blauensteiner, B., ukowski, M., Aspelmeyer, M. & Zeilinger, A. Experimental Interference of Independent Photons. *Physical Review Letters* **96**, 240502 (2006). URL http://link.aps.org/doi/10.1103/PhysRevLett.96.240502. 2

[14] Legero, T., Wilk, T., Hennrich, M., Rempe, G. & Kuhn, A. Quantum Beat of Two Single Photons. *Physical Review Letters* **93**, 070503 (2004). URL http://link.aps.org/doi/10.1103/PhysRevLett.93.070503. 2

[15] Beugnon, J. *et al.* Quantum interference between two single photons emitted by independently trapped atoms. *Nature* **440**, 779–82 (2006). URL http://www.ncbi.nlm.nih.gov/pubmed/16598253. 2

[16] Santori, C., Fattal, D., Vucković, J., Solomon, G. S. & Yamamoto, Y. Indistinguishable photons from a single-photon device. *Nature* **419**, 594–7 (2002). URL http://www.ncbi.nlm.nih.gov/pubmed/12374958. 2

[17] Patel, R., Bennett, A., Farrer, I. & Nicoll, C. Two-photon interference of the emission from electrically tunable remote quantum dots. *Nature Photonics* **4**, 632–635 (2010). URL http://dx.doi.org/10.1038/nphoton.2010.161http://www.nature.com/nphoton/journal/v4/n9/abs/nphoton.2010.161.html. 2

[18] Kiraz, a. *et al.* Indistinguishable Photons from a Single Molecule. *Physical Review Letters* **94**, 223602 (2005). URL http://link.aps.org/doi/10.1103/PhysRevLett.94.223602. 2

[19] Lettow, R. *et al.* Quantum Interference of Tunably Indistinguishable Photons from Remote Organic Molecules. *Physical Review Letters* **104**, 123605 (2010). URL http://link.aps.org/doi/10.1103/PhysRevLett.104.123605. 2

[20] Maunz, P. *et al.* Quantum interference of photon pairs from two remote trapped atomic ions. *Nature Physics* **3**, 538–541 (2007). URL http://www.nature.com/doifinder/10.1038/nphys644. 2

[21] Chanelière, T. *et al.* Quantum Interference of Electromagnetic Fields from Remote Quantum Memories. *Physical Review Letters* **98**, 113602 (2007). URL http://link.aps.org/doi/10.1103/PhysRevLett.98.113602. 2

[22] Bernien, H. *et al.* Two-Photon Quantum Interference from Separate Nitrogen Vacancy Centers in Diamond. *Physical Review Letters* **108**, 043604 (2012). URL http://link.aps.org/doi/10.1103/PhysRevLett.108.043604. 2

[23] Lang, C. *et al.* Correlations, indistinguishability and entanglement in HongOuMandel experiments at microwave frequencies. *Nature Physics* **9**, 345–348 (2013). URL http://www.nature.com/doifinder/10.1038/nphys2612. 2

[24] Polyakov, S. V. *et al.* Coalescence of Single Photons Emitted by Disparate Single-Photon Sources: The Example of InAs Quantum Dots and Parametric Down-Conversion Sources. *Physical Review Letters* **107**, 157402 (2011). URL http://link.aps.org/doi/10.1103/PhysRevLett.107.157402. 2, 46, 49

[25] McMillan, A. R. *et al.* Two-photon interference between disparate sources for quantum networking. *Scientific reports* **3**, 2032 (2013). URL http://www.pubmedcentral.nih.gov/articlerender.fcgi?artid=3687221&tool=pmcentrez&rendertype=abstract. 2, 46, 49

[26] Srivathsan, B. *et al.* Narrow Band Source of Transform-Limited Photon Pairs via Four-Wave Mixing in a Cold Atomic Ensemble. *Physical Review Letters* **111**, 123602 (2013). URL http://link.aps.org/doi/10.1103/PhysRevLett.111.123602. 2, 22, 24, 25, 27

[27] Steck, D. Quantum and atom optics. *http://steck.us/teaching (revision 0.8.2, 6 December 2013)* URL http://atomoptics.uoregon.edu/~dsteck/teaching/quantum-optics/. 3, 63

[28] Grynberg, G., Aspect, A. & Fabre, C. *Introduction to quantum optics: from the semi-classical approach to quantized light* (Cambridge Unviersity Press, 2010). 3

[29] Kurtsiefer, C. & Linares, A. L. Quantum information processing and quantum optics devices. In *Ultracold Gases and Quantum Information: Ultracold Gases and Quantum Information: Lecture Notes of the Les Houches Summer School in Singapore: Volume 91, July 2009* (2009). 3

[30] Bennett, C. H. & Brassard, G. Quantum Cryptography: Public Key Distribution and Coin Tossing. In *Internation Conference on Computers, Systems & Signal Processing* (India, 1984). URL http://www.cs.ucsb.edu/~chong/290N-W06/BB84.pdf. 3

[31] Bennett, C. H., Bessette, F., Brassard, G., Salvail, L. & Smolin, J. Experimental quantum cryptography. *Journal of Cryptology* **5** (1992). URL http://link.springer.com/10.1007/BF00191318. 3

[32] Scarani, V. *et al.* The security of practical quantum key distribution. *Reviews of Modern Physics* **81**, 1301–1350 (2009). URL http://link.aps.org/doi/10.1103/RevModPhys.81.1301. 3

[33] Jennewein, T., Achleitner, U., Weihs, G., Weinfurter, H. & Zeilinger, A. A fast and compact quantum random number generator. *Review of Scientific Instruments* **71**, 1675 (2000). URL http://scitation.aip.org/content/aip/journal/rsi/71/4/10.1063/1.1150518. 4

[34] Stefanov, A., Gisin, N., Guinnard, O., Guinnard, L. & Zbinden, H. Optical quantum random number generator. *Journal of Modern Optics* **47**, 595–598 (2000). URL http://dx.doi.org/10.1080/09500340008233380. 4

[35] Lounis, B. & Orrit, M. Single-photon sources. *Reports on Progress in Physics* **68**, 1129–1179 (2005). URL http://stacks.iop.org/0034-4885/68/i=5/a=R04?key=crossref.a93d907e49621855b101f96e0a36e3d6. 4

[36] Giovannetti, V., Lloyd, S. & Maccone, L. Quantum-enhanced positioning and clock synchronization. *Nature* **412**, 417–9 (2001). URL http://dx.doi.org/10.1038/35086525. 4

[37] Eisaman, M. D., Fan, J., Migdall, a. & Polyakov, S. V. Invited review article: Single-photon sources and detectors. *The Review of scientific instruments* **82**, 071101 (2011). URL http://www.ncbi.nlm.nih.gov/pubmed/21806165. 4

[38] Hijlkema, M. *et al.* A single-photon server with just one atom. *Nature Physics* **3**, 253–255 (2007). URL http://www.nature.com/doifinder/10.1038/nphys569. 4

[39] Kuhn, A., Hennrich, M. & Rempe, G. Deterministic Single-Photon Source for Distributed Quantum Networking. *Physical Review Letters* **89**, 067901 (2002). URL http://link.aps.org/doi/10.1103/PhysRevLett.89.067901. 4

[40] Hennrich, M., Legero, T., Kuhn, a. & Rempe, G. Photon statistics of a non-stationary periodically driven single-photon source. *New Journal of Physics* **6**, 86–86 (2004). URL http://stacks.iop.org/1367-2630/6/i=1/a=086?key=crossref.1bf221f4ebad385995d272ac07ccc77f. 4

[41] Wilk, T., Webster, S., Specht, H., Rempe, G. & Kuhn, a. Polarization-Controlled Single Photons. *Physical Review Letters* **98**, 063601 (2007). URL http://link.aps.org/doi/10.1103/PhysRevLett.98.063601. 4

[42] McKeever, J. *et al.* Deterministic generation of single photons from one atom trapped in a cavity. *Science (New York, N.Y.)* **303**, 1992–4 (2004). URL http://www.ncbi.nlm.nih.gov/pubmed/14988512. 4

[43] Darquié, B. *et al.* Controlled single-photon emission from a single trapped two-level atom. *Science (New York, N.Y.)* **309**, 454–6 (2005). URL http://www.ncbi.nlm.nih.gov/pubmed/16020731. 5

[44] Aljunid, S. A. *et al.* Excitation of a Single Atom with Exponentially Rising Light Pulses. *Physical Review Letters* **111**, 103001 (2013). URL http://link.aps.org/doi/10.1103/PhysRevLett.111.103001. 5

[45] Malinovsky, V. & Krause, J. General theory of population transfer by adiabatic rapid passage with intense , chirped laser pulses. *The European Physical Journal D* **155**, 147–155 (2001). URL http://link.springer.com/article/10.1007/s100530170212. 5

[46] Metcalf, H. & van der Straten, P. *Laser cooling and trapping* (Springer Science, 1999). 5, 7

[47] Hood, C. J., Chapman, M. S., Lynn, T. W. & Kimble, H. J. Real-Time Cavity QED with Single Atoms. *Physical Review Letters* **80**, 4157–4160 (1998). URL http://link.aps.org/doi/10.1103/PhysRevLett.80.4157. 6

[48] Tey, M. K. *et al.* Strong interaction between light and a single trapped atom without the need foracavity. *Nature Physics* **4**, 924–927 (2008). URL http://www.nature.com/doifinder/10.1038/nphys1096. 6, 8, 14

[49] Schlosser, N., Reymond, G. & Grangier, P. Collisional Blockade in Microscopic Optical Dipole Traps. *Physical Review Letters* **89**, 023005 (2002). URL http://link.aps.org/doi/10.1103/PhysRevLett.89.023005. 8

[50] Schlosser, N., Reymond, G., Protsenko, I. & Grangier, P. Sub-poissonian loading of single atoms in a microscopic dipole trap. *Nature* **411**, 1024–7 (2001). URL http://www.ncbi.nlm.nih.gov/pubmed/11429597. 8

[51] Steck, D. A. Rubidium 87 D Line Data. Tech. Rep. (2003). URL http://steck.us/alkalidata. 15

[52] Volz, U. & Schmoranzer, H. Precision lifetime measurements on alkali atoms and on helium by beamgaslaser spectroscopy. *Physica Scripta* **48** (1996). URL http://iopscience.iop.org/1402-4896/1996/T65/007. 20

[53] Feichtner, J., Gallagher, J. & Mizushima, M. Lifetime of the First Excited Atomic States of Rb87. *Physical Review* **164** (1967). URL http://prola.aps.org/abstract/PR/v164/i1/p44_1. 20

[54] Rotberg, E. a. *et al.* Measurement of excited-state lifetime using two-pulse photon echoes in rubidium vapor. *Journal of the Optical Society of America B* **24**, 671 (2007). URL http://www.opticsinfobase.org/abstract.cfm?URI=josab-24-3-671. 20

[55] Boyd, R. W. *Nonlinear Optics*, vol. 2003 (Elsevier Science (USA), 2003). URL http://books.google.com/books?hl=fr&lr=&id=3vHb7WGXmSQC&pgis=1. 24

[56] Kurtsiefer, C., Oberparleiter, M. & Weinfurter, H. High-efficiency entangled photon pair collection in type-II parametric fluorescence. *Physical Review A* **64**, 023802 (2001). URL http://link.aps.org/doi/10.1103/PhysRevA.64.023802. 24

[57] Wong, F. N. C., Shapiro, J. H. & Kim, T. Efficient generation of polarization-entangled photons in a nonlinear crystal. *Laser Physics* **16**, 1517–1524 (2006). URL http://link.springer.com/10.1134/S1054660X06110053. 24

[58] Förtsch, M. *et al.* A versatile source of single photons for quantum information processing. *Nature communications* **4**, 1818 (2013). URL http://www.ncbi.nlm.nih.gov/pubmed/23652006. 24

[59] Wolfgramm, F. *et al.* Bright filter-free source of indistinguishable photon pairs Abstract : **16**, 18145–18151 (2008). 24

[60] Haase, A., Piro, N., Eschner, J. & Mitchell, M. W. Tunable narrowband entangled photon pair source for resonant single-photon single-atom interaction **34**, 55–57 (2009). 24

[61] Li, X., Voss, P., Sharping, J. & Kumar, P. Optical-Fiber Source of Polarization-Entangled Photons in the 1550nm Telecom Band. *Physical Review Letters* **94**, 053601 (2005). URL http://link.aps.org/doi/10.1103/PhysRevLett.94.053601. 24

[62] Smith, B. J., Mahou, P., Cohen, O., Lundeen, J. S. & Walmsley, I. a. Photon pair generation in birefringent optical fibers. *Optics express* **17**, 23589–602 (2009). URL http://www.ncbi.nlm.nih.gov/pubmed/20052068. 24

[63] Chanelière, T. *et al.* Quantum Telecommunication Based on Atomic Cascade Transitions. *Physical Review Letters* **96**, 093604 (2006). URL http://link.aps.org/doi/10.1103/PhysRevLett.96.093604. 24

[64] Willis, R. T., Becerra, F. E., Orozco, L. a. & Rolston, S. L. Photon statistics and polarization correlations at telecommunications wavelengths from a warm atomic ensemble. *Optics express* **19**, 14632–41 (2011). URL http://www.ncbi.nlm.nih.gov/pubmed/21934825. 24

[65] Ding, D.-S., Zhou, Z.-Y., Shi, B.-S., Zou, X.-B. & Guo, G.-C. Generation of non-classical correlated photon pairs via a ladder-type atomic configuration: theory and experiment. *Optics express* **20**, 11433–44 (2012). URL http://www.ncbi.nlm.nih.gov/pubmed/22565763. 24

[66] Dicke, R. Coherence in spontaneous radiation processes. *Physical Review* **93**, 99–110 (1954). URL http://journals.aps.org/pr/abstract/10.1103/PhysRev.93.99. 25

[67] Rehler, N. & Eberly, J. Superradiance. *Physical Review A* **3** (1971). URL http://journals.aps.org/pra/abstract/10.1103/PhysRevA.3.1735. 25

[68] Loudon, R. *The quantum theory of light* (Oxford University Press, 2000), 3 edn. URL http://scholar.google.com/scholar?hl=fr&q=loudon+quantum+theory+of+light&btnG=&lr=#0. 30, 31

[69] Simon, C. & Irvine, W. Robust Long-Distance Entanglement and a Loophole-Free Bell Test with Ions and Photons. *Physical Review Letters* **91**, 110405 (2003). URL http://link.aps.org/doi/10.1103/PhysRevLett.91.110405. 49

[70] Srivathsan, B., Gulati, G. K., Cerè, A., Chng, B. & Kurtsiefer, C. Reversing the Temporal Envelope of a Heralded Single Photon using a Cavity. *Physical Review Letters* **113**, 163601 (2014). URL http://link.aps.org/doi/10.1103/PhysRevLett.113.163601. 49

[71] Cohen-Tannoudji, C., Dupont-Roc, J. & Grynberg, G. *Atom-Photon Interactions: Basic Processes and Applications* (WILEY-VCH, 2004). 63

[72] Weisskopf, V. & Wigner, E. Berechnung der natürlichen linienbreite auf grund der diracschen lichttheorie. *Zeitschrift für Physik* 54–73 (1930). URL `http://link.springer.com/article/10.1007/BF01336768`. 67

Appendix A

Additional Information for Chapter 2

A.1 The Probability of the Atom in the Excited State $P_e(t)$

This section details the conversion from the normalised counts $N(t)$, as defined in (2.1), to the probability of the atom in the excited state $P_e(t)$ used in Fig. 2.11.

According to the Wigner-Weiskopf treatment, the interaction between a two-level system with the vacuum radiation mode causes the excited state to decay to the ground state with a certain decay rate Γ that depends on the coupling strength between the two-level system with the environment. The probability $P_e(t)$ decays according to the following relation (refer to Appendix B.2)

$$\frac{dP_e(t)}{dt} = -\Gamma P_e(t)$$

The rate of change of $P_e(t)$ can be inferred from the number of photons emitted between time t and $t + dt$ as shown by the following relation.

$$\begin{aligned} P_e(t) &= -\frac{1}{\Gamma}\frac{dP_e(t)}{dt} \\ &\approx -\frac{1}{\Gamma}\frac{P_e(t+\Delta t) - P_e(t)}{\Delta t} \\ &\approx \frac{1}{\Gamma}\frac{N(t)}{\eta_d \eta_s \Delta t}, \end{aligned}$$

with η_d being the detection efficiency (~ 0.3) that takes into account the coupling efficiency into the fiber coupler and the quantum efficiency of the APD. The spatial overlap η_s (~ 0.03) is a measure of the overlap between the collection mode and the emission mode of the atom.

A.2 Uncertainty in the Total Excitation Probability P_E

This section details the calculation of the uncertainty in the total excitation probability. The total excitation probability of the atom P_E is defined in (2.2).

The uncertainty in the total excitation probability (ΔP_E) shown in Fig. 2.12 consists of the uncertainty due to the Poissonian counting statistics (ΔP_{poiss}) and also the timing uncertainty (ΔP_t).

$$\Delta P_E = \Delta P_{poiss} + \Delta P_t$$

The timing uncertainty is attributed to the jitter time of the detector itself that is in the order of 1 ns. This causes an error in the determination of t_i and t_f. The uncertainty ΔP_t is calculated as follows:

$$\Delta P_t = \frac{1}{\eta}\sqrt{\sigma_{t_i}^2\left(\frac{\partial A(t_i,t_f)}{\partial t_i}\right)^2 + \sigma_{t_f}^2\left(\frac{\partial A(t_i,t_f)}{\partial t_f}\right)^2}, \tag{A.1}$$

where σ_{t_i} and σ_{t_f} are the timing uncertainties (1 ns), and η is the overall detection and collection efficiency. The partial derivatives are calculated by discretizing each of them in time. Due to the choice of t_f, the contribution of the second term in ΔP_t is negligible with respect to the first term. Therefore, ΔP_t approximates to

$$\begin{aligned}\Delta P_t &\approx \frac{1}{\eta}\sigma_{t_i}\left(\frac{\partial A(t_i,t_f)}{\partial t_i}\right)\\ &\approx \frac{1}{\eta}\times 1\text{ ns}\times\frac{1}{2}\left(\frac{|A(t_i-1\text{ ns},t_f)-A(t_i,t_f)|}{1\text{ ns}}+\frac{|A(t_i+1\text{ ns},t_f)-A(t_i,t_f)|}{1\text{ ns}}\right)\end{aligned}$$

Note that the uncertainty shown in Fig. 2.11 does not take into account the uncertainty in the overall detection and collection efficiency η, estimated to be $\approx 2\times 10^{-3}$.

Appendix B

Theory of Atom-Light Interaction

The subject of atom-light interaction has been discussed in great detail in [27, 71]. The treatment presented here follows closely [27].

Here, we will restrict our discussion to the description of an atom as a two-level system. Although this is not typically the case in real atoms, some elements do possess closed cycling transitions. This allows us to approximate a multi-level atom as an effective two-level system.

In the first part, we examine the dynamics of a two-level system in the presence of external light. In the second part, we examine the situation where an excited two-level system in the absence of external light decays to the ground state due to the interaction with the vacuum radiation modes.

B.1 Excitation of a Two-Level System

Consider the following problem of an electron in a two-level system interacting with excitation light as shown in Fig. B.1.

The transition frequency between the ground state $|g\rangle$ and the excited state $|e\rangle$ is denoted as $\omega_0 = |E_e - E_g|/\hbar$. The electric field of the excitation light is assumed to be of the form $\vec{E}(t) = E_0 \cos(\omega t)\vec{\epsilon}$, with frequency ω, polarization vector $\vec{\epsilon}$ ($|\vec{\epsilon}| = 1$) and is treated as a classical field for simplicity. We use the long-wavelength or dipole approximation where the light's wavelength is assumed to be much larger than the size of the atom. In this approximation, the amplitude of the excitation light over the atom can be approximated as a constant, E_0.

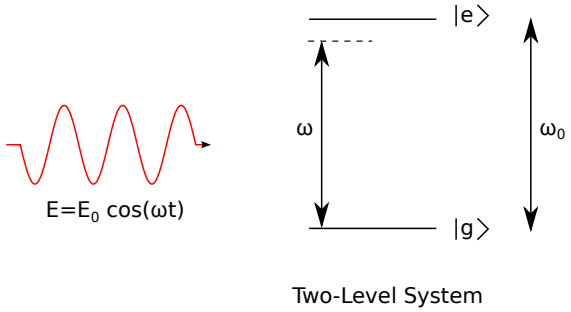

Figure B.1: Two-level system interacting with light.

The total Hamiltonian of the two-level system under the dipole approximation is

$$\hat{H} = \hat{H}_{atom} + \hat{H}_{dip}\,, \tag{B.1}$$

where the atomic free-evolution Hamiltonian is

$$\hat{H}_{atom} = \hbar\omega_0 |e\rangle\langle e|\,.$$

The energy levels are defined such that the ground state has zero energy. The dipolar interaction Hamiltonian is

$$\begin{aligned}\hat{H}_{dip} &= -\vec{\hat{d}}\cdot\vec{E}(t) \\ &= -\left(\vec{\hat{d}}\cdot\vec{\epsilon}\right)E_0\cos(\omega t)\,.\end{aligned}$$

The atomic dipole operator is the product between the charge of the electron and the position operator of the electron, i.e. $\vec{\hat{d}} = -e\vec{\hat{r}}_e$. In the eigenstates of the free-evolution Hamiltonian, the atomic dipole operator can be expressed as

$$\vec{\hat{d}} = \left[\vec{d}_{ge}\right]|g\rangle\langle e| + \left[\vec{d}_{ge}\right]^*|e\rangle\langle g|\,,$$

where $\vec{d}_{ge} = \langle g|\vec{\hat{d}}|e\rangle$ is nonvanishing only if $|e\rangle$ and $|g\rangle$ are of opposite parity. Here, the matrix element $\vec{d}_{ge}$ is chosen to be real.

The state of the atom $|\psi(t)\rangle$ at any later time t can also be expressed as

$$|\psi(t)\rangle = c_g(t)|g\rangle + c_e(t)e^{-i\omega_0 t}|e\rangle \tag{B.2}$$

The coefficients $c_g(t)$ and $c_e(t)$ can be found by solving the Schrödinger equation using the Hamiltonian in (B.1) and the state decomposition above (B.2). In the rotating

wave approximation, i.e. $|\omega - \omega_0| \ll (\omega + \omega_0)$, the Schrödinger equation reduces to

$$i\hbar \frac{d|\psi(t)\rangle}{dt} = \hat{H}|\psi(t)\rangle \rightarrow \left\{ \begin{array}{l} i\hbar \dfrac{dc_g(t)}{dt} = \dfrac{\Omega_1}{2} c_e(t) e^{i(\omega-\omega_0)t} \\ \\ i\hbar \dfrac{dc_e(t)}{dt} = \dfrac{\Omega_1}{2} c_g(t) e^{-i(\omega-\omega_0)t} \end{array} \right\},$$

with $\Omega_1 = \left(\vec{d}_{ge} \cdot \vec{\epsilon}\right) E_0/\hbar$ being defined as the *Rabi frequency* and is defined such that $\Omega_1 > 0$. Note that the Rabi frequency is proportional to the amplitude of the electric field.

We define the detuning of the external light with respect to the atomic transition as $\Delta\omega := \omega - \omega_0$. The solution to the coupled differential equations above for an arbitrary initial state $(c_g(0), c_e(0))$ is

$$\begin{aligned} c_g(t) &= e^{i\Delta\omega t/2}\left[c_g(0)\cos\left(\frac{\Omega}{2}t\right) - \frac{i}{\Omega}\left(c_e(0)\Omega_1 + c_g(0)\Delta\omega\right)\sin\left(\frac{\Omega}{2}t\right)\right] \\ c_e(t) &= e^{-i\Delta\omega t/2}\left[c_e(0)\cos\left(\frac{\Omega}{2}t\right) - \frac{i}{\Omega}\left(c_g(0)\Omega_1 + c_e(0)\Delta\omega\right)\sin\left(\frac{\Omega}{2}t\right)\right], \end{aligned} \tag{B.3}$$

with $\Omega = \sqrt{\Omega_1^2 + \Delta\omega^2}$ defined as the generalized Rabi frequency. In the following, we illustrate three special cases that are of interest to us.

Example 1: For a two-level system initially prepared in the ground state $(c_g(0) = 1, c_e(0) = 0)$ and excitation light of constant amplitude, the probability of finding the system in the excited state as a function of time is

$$P_e(t) = |c_e(t)|^2 = \frac{\Omega_1^2}{\Omega^2}\sin^2\left(\frac{\Omega}{2}t\right)$$

The population of the excited state oscillates with frequency Ω. This oscillation is usually referred to as the *Rabi oscillation*. The maximum value of $P_e(t)$ occurs when $\Omega T = \pi$ for a value of $P_{e,max} = \Omega_1^2/\Omega^2$ which is equal to 1 for excitation light at resonant with the transition frequency. An optical pulse of this duration $(T = \pi/\Omega)$ is usually referred to as a π pulse. In other words, a π pulse is the shortest optical pulse required to achieve the highest probability of the atom being in the excited state.

Example 2 : If the atom is initially prepared in the excited state $(c_g(0) = 0, c_e(0) = 1)$, then the probability of the atom being in the ground state is

$$P_g(t) = \frac{\Omega_1^2}{\Omega^2}\sin^2\left(\frac{\Omega}{2}t\right) \tag{B.4}$$

In particular, this result predicts that the atom will stay in the excited state forever if there is no excitation light for $t \geq 0$. Note that this is not the case in reality, where the atom will decay to the ground state through spontaneous emission. This will be detailed in the next section.

Example 3: Consider the special case where the excitation light is on resonance with the transition frequency ($\Delta\omega = 0$). If the amplitude of the light slowly fluctuates in time, ie. $\Omega_1 = \Omega_1(t)$, the requirement to get the π pulse can be generalized to

$$\int_0^T \Omega_1(t)dt = \pi$$

To illustrate this, consider the evolution of the atomic state interacting with an excitation light at resonance for an infinitesimal time step dt at time t. During this time interval, the Rabi frequency can be regarded as a constant. The coefficients $c_g(t+dt)$ and $c_e(t+dt)$ in (B.3) can be expressed as

$$\begin{pmatrix} c_g(t+dt) \\ c_e(t+dt) \end{pmatrix} = \underbrace{\begin{pmatrix} \cos\left(\frac{\Omega_1(t)}{2}dt\right) & -i\sin\left(\frac{\Omega_1(t)}{2}dt\right) \\ -i\sin\left(\frac{\Omega_1(t)}{2}dt\right) & \cos\left(\frac{\Omega_1(t)}{2}dt\right) \end{pmatrix}}_{[\hat{U}(t,t+dt)]} \begin{pmatrix} c_g(t) \\ c_e(t) \end{pmatrix}$$

The matrix $\left[\hat{U}(t,t+dt)\right]$ above is a unitary operator written in the basis of the free-evolution Hamiltonian, i.e. $\hat{H}_{atom}$. Expressed in terms of Pauli matrices, then

$$\hat{U}(t,t+dt) = \exp\left[-i\frac{\Omega_1(t)dt}{2}\hat{\sigma}_x\right]$$

where $\hat{\sigma}_x = |e\rangle\langle g| + |g\rangle\langle e|$. In the picture of a Bloch sphere, this corresponds to an infinitesimal rotation of the state vector by an angle $\frac{\Omega_1(t)}{2}dt$ with the x-axis being the axis of rotation. Therefore the cumulative effect of slowly fluctuating light's amplitude can be understood as being composed of a series of rotations around the x-axis, each time a different rotation angle ($d\theta = \Omega(t)dt$).

$$\begin{aligned} \hat{U}(0,T) &= \hat{U}(0,dt)\hat{U}(dt,2dt)...\hat{U}(t,t+dt)...\hat{U}(T-dt,T) \\ &= \exp\left[-\frac{i}{2}\underbrace{\left(\int_0^T \Omega_1(t')dt'\right)}_{\Theta}\hat{\sigma}_x\right] \end{aligned}$$

A π pulse therefore corresponds to $\Theta = \pi$ in this example. This is relevant in the scenario where the field amplitude is not constant but a full excitation can still be accomplished.

B.2 Spontaneous Emission in Free Space

Consider a two-level system in the excited state at $t = 0$ as shown in Fig. B.2. The result derived in example 2 of the previous section predicts that the system will stay in the excited state forever if there is no external light to perturb this equilibrium. However, this is not observed in reality where the excited state actually decays to the ground state even if there is no external light to interact with. To explain such observations, one needs to take into account the interaction between the two-level system with all the vacuum radiation modes. This calls for a full quantum treatment of both the two-level system and the radiation modes. The following discussion follows the treatment of Weisskopf and Wigner [72].

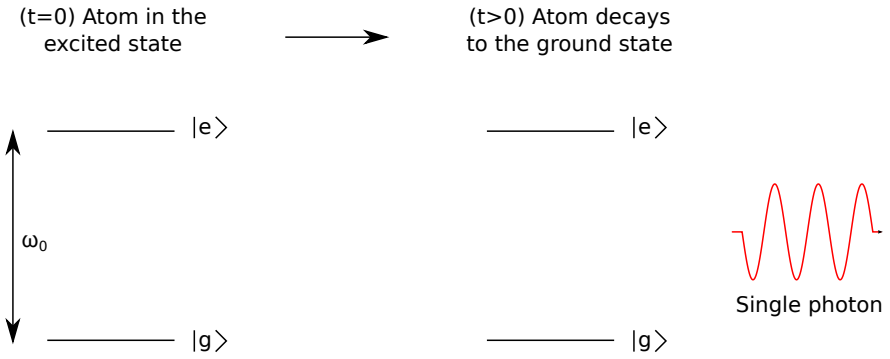

Figure B.2: Atom initially prepared in the excited state decays to the ground state through spontaneous emission emitting a single photon.

The electron - electromagnetic field interaction is assumed to be mainly dominated by the electric dipolar interaction. The total Hamiltonian of the atom-light system under the rotating wave approximation is

$$\hat{H} = \hat{H}_{atom} + \hat{H}_{field} + \hat{H}_{dip}\,, \tag{B.5}$$

with

$$\begin{aligned}
\hat{H}_{atom} &= \hbar\omega_0 |e\rangle\langle e| \otimes \mathbb{1}_{field} \\
\hat{H}_{field} &= \mathbb{1}_{atom} \otimes \sum_{\{\vec{k},s\}} \hbar\omega_k (\hat{a}^\dagger \hat{a})_{\{\vec{k},s\}} \\
\hat{H}_{dip} &= -\hat{\vec{d}} \cdot \hat{\vec{E}} = \sum_{\{\vec{k},s\}} \hbar g_{\{\vec{k},s\}} |e\rangle\langle g| \otimes \hat{a}_{\{\vec{k},s\}} + h.c
\end{aligned}$$

In free space, we can consider a quantization cubic box of volume V with a periodic boundary condition. For such boundary condition, each radiation mode can be characterized by a wavevector $\vec{k}$ and the polarization $s = \{1, 2\}$. The annihilation and creation operators of the radiation mode $\{\vec{k}, s\}$ are denoted by $\hat{a}_{\{\vec{k},s\}}$ and $\hat{a}^{\dagger}_{\{\vec{k},s\}}$, respectively. The coupling factor $g_{\{\vec{k},s\}}$ is defined as

$$g_{\{\vec{k},s\}} = -\sqrt{\frac{\omega_k}{2\epsilon_0 \hbar V}}\vec{d}_{ge} \cdot \vec{\epsilon}_{\{\vec{k},s\}}$$

Expressed in the basis of the uncoupled atom-field system, the initial state can be written as $|\psi(0)\rangle = |e, \{0\}\rangle$ where, $|\{0\}\rangle$ denotes that all the radiation modes are in vacuum state. From the form of the interaction Hamiltonian, the state of the atom-field system at any later time can be expressed as

$$|\psi(t)\rangle = c_e(t)e^{-i\omega_0 t}|e, \{0\}\rangle + \sum_{\vec{k},s} c_{\{\vec{k},s\}}(t)e^{-i\omega_k t}|g, 1_{\{\vec{k},s\}}\rangle\,, \tag{B.6}$$

where the state $|1_{\{\vec{k},s\}}\rangle$ denotes the radiation mode $\{\vec{k}, s\}$ having one photon and the rest are in vacuum mode. By solving the Schrödinger equation using the state decomposition in (B.6) and Hamiltonian in (B.5), this results in two coupled differential equations.

$$i\hbar\frac{d|\psi(t)\rangle}{dt} = \hat{H}|\psi(t)\rangle \rightarrow \left\{ \begin{array}{ll} \dfrac{dc_e(t)}{dt} & = -i\sum_{\{\vec{k},s\}} g_{\{\vec{k},s\}} c_{\{\vec{k},s\}}(t)e^{-i(\omega_k-\omega_0)t} \\ \dfrac{dc_{\{\vec{k},s\}}(t)}{dt} & = -ig^{*}_{\{\vec{k},s\}} c_e(t)e^{i(\omega_k-\omega_0)t} \end{array} \right\}$$

From the second equation, the coefficient $c_{\{\vec{k},s\}}(t)$ can be expressed in integral form and can be in turn used to solve for $c_e(t)$. This results in

$$\frac{dc_e(t)}{dt} = -\sum_{\{\vec{k},s\}} |g_{\{\vec{k},s\}}|^2 \int_0^t dt' c_e(t')e^{-i(\omega_k-\omega_0)(t-t')} \tag{B.7}$$

To solve this integro-differential equation, one can make several approximations. First of all, the amplitude $c_e(t)$ is assumed to vary slowly compared to the exponential term. For $t' < t$, the exponential term that oscillates rapidly is negligible except when $t' = t$. As such, we can approximate the value of $c_e(t')$ as a constant and replace it by its value at time t, i.e. $c_e(t)$. Since there is also little contribution from $t' > t$, one can extend the integration limit to infinity. Denote $\tau = t - t'$, then

$$\begin{aligned} \int_0^t e^{-i(\omega_k-\omega_0)(t-t')}c_e(t')dt' &\approx c_e(t)\int_0^{\infty} d\tau e^{-i(\omega_k-\omega_0)\tau} \\ &= c_e(t)\pi\delta(\omega_k-\omega_0) \end{aligned}$$

For the summation over the modes $\{\vec{k}, s\}$ in (B.7), we can extend the volume of the quantization box to infinity. In this limit, the spacing between modes becomes smaller and the summation can be replaced by an integral.

$$\sum_{\{\vec{k},s\}} |g_{\{\vec{k},s\}}|^2 \xrightarrow[V\to\infty]{} \int \frac{V}{(2\pi)^3} d\vec{k} \sum_s \frac{\omega_k}{2\epsilon_0 \hbar V} |\vec{d}_{ge} \cdot \vec{\epsilon}_{\{\vec{k},s\}}|^2$$

Denote the angle between the $\vec{k}$ and $\vec{d}_{ge}$ as θ. In free space, the wavevector $\vec{k}$ and the two orthogonal polarization vectors $\vec{\epsilon}_{\{\vec{k},1\}}$, $\vec{\epsilon}_{\{\vec{k},2\}}$ form an orthogonal basis from which any vector, including the electric dipole moment $\vec{d}_{ge}$ can be expanded. Therefore,

$$\sum_{s=1,2} |\vec{d}_{ge} \cdot \vec{\epsilon}_{\{\vec{k},s\}}|^2 = |\vec{d}_{ge}|^2 (1 - \cos^2\theta) = |\vec{d}_{ge}|^2 \sin^2\theta$$

Combining these results and recalling the dispersion relation $\omega_k = ck$, (B.7) becomes

$$\begin{aligned}
\frac{dc_e(t)}{dt} &= -\left(\sum_{\{\vec{k},s\}} |g_{\{\vec{k},s\}}|^2 \right) \times \left(\int_0^t dt' c_e(t') e^{-i(\omega_k - \omega_0)(t-t')} \right) \\
&= -\left(\int \frac{1}{(2\pi)^3} d\vec{k} \frac{\omega_k}{2\epsilon_0 \hbar} |\vec{d}_{ge}|^2 \sin^2\theta \right) \times \pi\delta(\omega_k - \omega_0) c_e(t) \\
&= -\left(\frac{|\vec{d}_{ge}|^2}{(2\pi)^2 2\epsilon_0 \hbar} \int_0^\infty k^2 dk \int_0^{2\pi} \sin^3\theta d\theta \right) \times \pi\delta(\omega_k - \omega_0) c_e(t) \\
&= -\frac{\omega_0^3 |\vec{d}_{ge}|^2}{3\pi\epsilon_0 \hbar c^3} \frac{c_e(t)}{2} \\
\frac{dc_e(t)}{dt} &= -\frac{\Gamma}{2} c_e(t)
\end{aligned}$$

The constant Γ defined as

$$\Gamma = \frac{\omega_0^3 |\vec{d}_{ge}|^2}{3\pi\epsilon_0 \hbar c^3}$$

is called the spontaneous decay rate and is defined such that the probability of the atom being in the excited state, i.e. $P_e(t) = |c_e(t)|^2$, decays exponentially at the rate of Γ.

$$\begin{aligned}
\frac{dP_e(t)}{dt} &= -\Gamma P_e(t) \\
P_e(t) &= P_e(0) e^{-\Gamma t}
\end{aligned}$$

Therefore a two-level atom initially prepared in the excited state will eventually decay to the ground state due to the interaction with the vacuum radiation modes.

The decay rate Γ depends on the dipole matrix element between the ground and the excited state ($|\vec{d}_{ge}|$) and also the resonant frequency of the optical transition (ω_0). This decay would give rise to the emission of a single photon with the probability being in mode $\{\vec{k}, s\}$ is equal to $|c_{\{\vec{k},s\}}|^2$. This phenomenon of the excited atom emitting a single photon in the absence of external light is referred to as the spontaneous emission.

Appendix C

Additional Information for Chapter 3

C.1 Matching the Delays between the Photons from Atomic Ensemble and Single Atom

In Section 3.3.2, we pointed out the need to operate the probe acousto-optic modulator (AOM) in "pulsing" mode. This is to increase the overall extinction ratio when the excitation pulses are not being generated.

Fig. C.1 shows the time delay between the optical output of the probe AOM and the output signal of the pattern generator. There is a 515 ns delay before the optical signal starts to rise and another 100 ns to reach the steady state. This is due to the acoustic transit time in the AOM and finite beam size. Due to the limited probe laser power available in the setup, we only want to generate the excitation pulse when the AOM response has reached its maximum amplitude at its steady state.

Therefore a minimum delay of 615 ns between the arrival of the four-wave mixing (FWM) trigger at the single atom (SA) setup and the arrival of the FWM photon is required. This is to match the arrival time of the SA photon and the FWM photon at the beam splitter in the HOM interferometer.

We use a long optical fiber that gives a 850 ns time delay between the arrival of the FWM trigger and the arrival of the FWM photon in the Hong-Ou-Mandel (HOM) interferometer. Further fine-tuning of the time delay between the two photons is done using the manual delay box shown in Fig. 3.2. This manual delay box basically delays

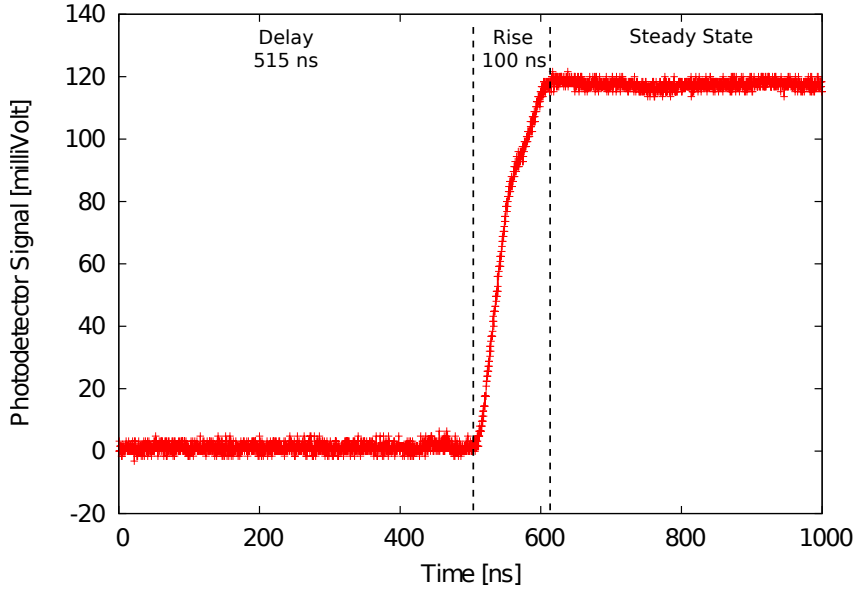

Figure C.1: Optical response of an AOM measured by a fast photodetector. The origin of the time axis represents the time at which the pattern generator outputs a command to turn on the AOM.

the arrival of the FWM trigger at the SA setup that, in turn, delays the excitation of the single atom.

C.2 The Estimation of Accidental Coincidences

This section discusses about the estimation of accidental coincidences in the measurement of the three-fold coincidences for the two-photon interference experiment. The major contribution to these accidentals can be associated with a click due to a single photon, either from SA or FWM, in one of the detectors, and an accidental click (the background counts and the dark counts of the detectors) in the other detector.

We define two 80 ns wide time windows for the detectors in the HOM interferometer. They are denoted as $W_{acc,i}$ and $W_{pho,i}$, where $i = 1, 2, 3$ denotes the detector. For instance, $W_{pho,1}$ is the time window where we expect to detect the single photons from either source at the detector D_1, and $W_{acc,1}$ the time window in D_1 where we expect to detect only the background floors as illustrated in Fig. C.2.

In this notation, the measured N_{012} is the number of three-fold coincidences between the FWM trigger, the click in D_1 within the time window $W_{pho,1}$ and the click in D_2

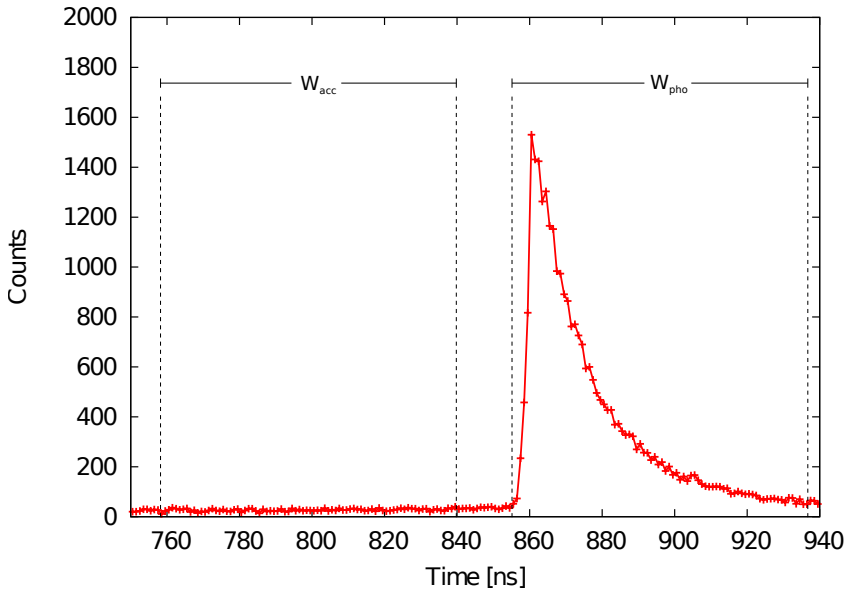

Figure C.2: Detection events in one of the HOM interferometer's detector (D_1 in Fig. 3.2) conditional on the arrival of the FWM trigger at the SA setup during the two-photon interference experiment when the two single photons overlap at the beam splitter (Δt_p = 0 ns). The time axis corresponds to the time delay between the arrival of the FWM trigger and the detection event in the detector. The data represented in this figure is basically the two-fold coincidences between the FWM trigger and the clicks in detector D_1, i.e. N_{01}. The two 80 ns coincidence windows, W_{pho} and W_{acc} are the two time windows used in the calculation of the accidentals. The data is processed in 1 ns time bins.

within the time window $W_{pho,2}$. The same applies to N_{013} and N_{023}.

For easy reference, the accidentals for the three-fold coincidence measurements are denoted as A_{012}, A_{013}, and A_{023} with the same naming convention for the subscripts as N_{012}, N_{013} and N_{023}. The total number of the FWM triggers that arrive at the single atom setup is N_0. The sum of the two-fold coincidences between the FWM trigger and the clicks in detector i within each coincidence window is denoted as

$$a_i = \sum_{W_{acc,i}} N_{0i}\,, \tag{C.1}$$

$$n_i = \sum_{W_{pho,i}} N_{0i}\,. \tag{C.2}$$

Then the accidentals are calculated as follows:

$$A_{0ij} \approx \left(\frac{n_i}{N_0}a_j + \frac{n_j}{N_0}a_i\right). \tag{C.3}$$

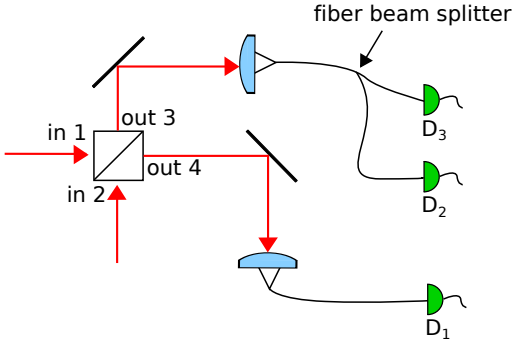

Figure C.3: Simplified illustration of the HOM interferometer. The two input ports are labelled 1 and 2. The two output ports are labelled 3 and 4.

The above calculation is based on the assumption that the background floor in the coincidence window W_{acc} represents well the background floor in the coincidence window W_{pho}.

C.3 Calculation of $\beta_\perp$ Using the Two-Fold Coincidences

In Section 3.5.2, we examined the HOM interference effect for different decay times of the four-wave mixing (FWM) photon. The decay time is varied by changing the average density of the atomic cloud. However, this would lead to different photon pair production efficiencies for different decay times. To compare the measurement results for different decay times, we have to rely on the quantity β defined as

$$\beta = \frac{N_{012} + N_{013}}{N_{023}} . \tag{C.4}$$

This quantity is independent of the photon pair production efficiency. Fig. 3.11 presents the result by comparing the ratio of β measured for $\parallel$ polarisations ($\beta_\parallel$) and the one measured for $\perp$ polarisations ($\beta_\perp$).

In this section, we want to show that in the $\perp$ case, the quantity $\beta_\perp$ can be calculated using the two-fold coincidences, i.e.

$$\frac{N_{012} + N_{013}}{N_{023}} = \frac{N_{01}(N_{02} + N_{03})}{N_{02}N_{03}} . \tag{C.5}$$

The key element here lies on the fact that for two input photons with $\perp$ polarisations, the beam splitter acts on one photon at one input independent of the photon at the other input. Therefore one should obtain the same distribution of counts at the three

detectors of the HOM interferometer if there is only one photon at one input and none at the other.

We first consider all the two-photon events conditional on the FWM triggers. We refer to Fig. C.3 as the reference figure. We define:

- $N(1_3, 1_4)$ as the number of two-photon events in which there is one photon at each output of beam splitter; $N(2_3, 0_4)$ as the number of two-photon events in which there are two photons at output 3 and no photon at output 4; $N(0_3, 2_4)$ as the number of two-photon events in which there are no photon at input 3 and two photons at output 4.

- T_1 as the transmission factor from the output 4 of the beam splitter to detector D_1; T_2, and T_3 as the transmission factors from output 3 to detector D_2 and D_3 respectively; This can be attributed to the mirror losses, coupling into the fiber, splitting ratio of the fiber beam splitter, detection efficiency, etc.

In term of the variables defined above, then the detected three-fold coincidences are:

$$N_{012} + N_{013} = N(1_3, 1_4) \times T_1(T_2 + T_3) \tag{C.6}$$

$$N_{023} = N(2_3, 0_4) \times 2T_2T_3 \tag{C.7}$$

The factor of 2 is due to the fact that there are two possibilities for the $(2_3, 0_4)$ events to be counted as coincidence events: either the first photon can go to D_2 and the second photon can go to D_3 or the first photon can go to D_3 and the other one can go to D_2. For clarity sake, if we suppose perfect detection efficiencies and no other loss mechanism, one would find $T_1 = 1$, [1]$T_2 = T_3 = 0.5$, $N_{012} + N_{013} = N(1_3, 1_4)$ and $N_{023} = N(2_3, 0_4)/2$.

For a 50:50 beam splitter and in the $\perp$ polarisations case, $\frac{N(1_3,1_4)}{2N(2_3,0_4)} = 1$ and

$$\beta_\perp = \frac{N_{012} + N_{013}}{N_{023}} = \frac{T_1(T_2 + T_3)}{T_2T_3} \tag{C.8}$$

Next, we consider all the one photon events conditional on the FWM triggers. We define:

[1]This is due to the splitting ratio of the fiber beam splitter that is assumed to be 50:50

- $N(1_3)$ as the total number of events with one photon at output 3 and no photon at output 4; $N(1_4)$ as the total number of events with no photon at output 3 and one photon at output 4.

Expressing the two-fold coincidences in terms of the variables defined above:

$$N_{01} = N(1_4)\,T_1\,, \tag{C.9}$$

$$N_{02} = N(1_3)\,T_2\,, \tag{C.10}$$

$$N_{03} = N(1_3)\,T_3\,. \tag{C.11}$$

For a 50:50 beam splitter, $\frac{N(1_4)}{N(1_3)} = 1$ and therefore $\frac{N(1_4)N(1_3)}{N(1_3)^2} = 1$. Thus

$$\beta = \frac{N_{01}(N_{02}+N_{03})}{N_{02}N_{03}} = \frac{T_1(T_2+T_3)}{T_2T_3}\,, \tag{C.12}$$

which is equal to (C.8). Therefore the value of $\beta_\perp$ can be calculated using the two-fold coincidences.